Elettore, E., Lettieri, A., Freddi, F., Latour, M., Rizzano, G. (2021). Performance-Based Assessment of Seismic-Resilient Steel Moment Resisting Frames Equipped with Innovative Column Bases Connections. Structures, 32: 1646–1664. https://doi.org/10.1016/j.istruc.2021.03.072

PERFORMANCE-BASED ASSESSMENT OF SEISMIC-RESILIENT STEEL MOMENT RESISTING FRAMES EQUIPPED WITH INNOVATIVE COLUMN BASE CONNECTIONS

Elena Elettore[1,*], Annarosa Lettieri[1], Fabio Freddi[2], Massimo Latour[1], Gianvittorio Rizzano[1]
[1]Department of Civil Engineering, University of Salerno
[2]Department of Civil, Environmental and Geomatic Engineering, University College London
[*]Corresponding Author. Tel.: +39 3276933946; E-mail address: eelettore@unisa.it

ABSTRACT

Many recent research studies have focused on developing innovative seismic-resilient structural systems to reduce repair costs and downtime in the aftermath of an earthquake. In this regard, dealing with steel Moment Resisting Frames (MRFs), recent research works have demonstrated the benefit deriving from the adoption of both low-damage and self-centring column base connections, both in terms of damage and residual drifts reduction. Although several technologies have been developed in this direction, only a few research studies investigated the significant parameters influencing the self-centring capability of these systems. Within this framework, the present study investigates the influence of the frame layout (*i.e.*, storeys and bays number) on the seismic performance, including the self-centring behaviour, of perimeter MRFs equipped with damage-free self-centring column bases previously studied by the authors. Nine case-study perimeter steel MRFs are designed and modelled in OpenSees. Incremental Dynamic Analyses are performed with a set of 30 ground motion records while monitoring both global and storey-level engineering demand parameters, including peak and residual interstorey drifts. Fragility curves are successively used to evaluate the self-centring capability of the structures. The present study provides insights on the use of the adopted connections for the residual drift reduction of MRFs and defines the boundaries of the investigated parameters for their application. Results highlight that the self-centring behaviour is particularly sensitive to the number of storeys and tends to reduce with the increasing height of MRFs equipped with the proposed connections.

KEYWORDS: Structural Resilience, Moment Resisting Steel frames, Self-centring, Damage-free column bases, Residual drifts.

1 INTRODUCTION

Conventional seismic design methods, suggested by most current codes and guidelines [*e.g.*, 1-3], and conventionally applied worldwide, are based on the exploitation of the local ductility of structural members or connections providing the development of a stable plasticization and the achievement of the safety requirements in case of 'rare' seismic events (*i.e.*, Ultimate Limit State). Such an approach implies extensive damage, often distributed throughout many non-replaceable structural elements, hence leading to large direct (*e.g.*, casualties, repair cost) and indirect (*e.g.*, downtime) losses [*e.g.*, 4]. To address this issue, during the past few decades, many analytical, numerical and experimental research studies have focused on the development of innovative structural systems, chasing the objectives of enhancing their seismic performance and resilience. These systems are often based on the inclusion of supplemental damping devices [*e.g.*, 5-12] or base isolation systems [*e.g.*, 13-15]. In the first case, the energy dissipation capacity is concentrated in a few, damage-free or easy-to-replace devices, while in the second case, the seismic demand is filtered by horizontally disconnecting the soil from the structure. These strategies offer the opportunity to preserve structural and non-structural components from damage, potentially leading to a significant reduction of repair cost and time in the aftermath of an earthquake.

For steel moment resisting frames (MRFs), several research studies, as well as practical applications have focused the attention on the replacement of conventional full-strength beam-to-column connections [*e.g.*, 16-22] and column bases (CBs) [*e.g.*, 23-27] with dissipative partial-strength joints, where dampers, such as friction devices (FDs) represent the dissipative elements of the connections [*e.g.*, 28-32]. These systems represent efficient solutions in protecting the frame from damage; nevertheless, they do not assure any control of the residual drifts, which could impair the building reparability after severe seismic events [33].

To address this issue, a wide variety of self-centring seismic-resisting systems has been developed over the past two decades. These are conventionally based on gap-opening mechanisms and the use of elastic restoring forces provided by high strength post-tensioned (PT) bars or strands [*e.g.*, 34-35]. In self-centring moment resisting frames (SC-MRFs) the gap opening is usually based on a rocking mechanism at the beam-to-column interface [*e.g.*, 36-39]. Beams are post-tensioned to the columns through high strength PT strands parallel to the beams and anchored outside the connection, allowing the control of the rocking mechanism. The dissipation of the seismic energy is provided by designated devices (*e.g.*, yielding seat angles [36], yielding buckling-restrained devices [37], friction devices [38] or yielding web hourglass pins [39]) which are included in the self-centring connection.

Other recent research works have been devoted to the development of damage-free self-centring CBs (SC-CBs) [*e.g.*, 40-50]. CBs represent fundamental components, whose behaviour significantly affects the seismic performance and repairability of the structure (*i.e.*, large plastic deformations [24, 25], axial shortening [26-27]) and hence, their protection is of paramount importance to achieve structural resilience. Several solutions for SC-CBs have been proposed in the last few years, based on the combination of rocking systems, dissipative devices and post-tensioned bars. Amongst others, Freddi *et al.* [46] presented and experimentally investigated [47] a rocking damage-free steel SC-CB equipped with FDs and high-strength steel PT bars. The main advances, respect to other similar studies, were related to the use of a circular steel plate with rounded edges as rocking base, preventing stress concentration and damage of the contact surfaces and allowing rocking towards all plan directions. Similarly, Kamperidis *et al.* [48] proposed a partial strength, low-damage, steel SC-CB equipped with PT tendons and hourglass shape steel yielding devices to dissipate the seismic energy. A similar approach was also followed by Wang *et al.* [49] while considering a concrete-filled square steel section as CB footing.

Moreover, Latour *et al.* [50] developed and experimentally investigated a SC-CB consisting of a slotted column splice where the seismic behaviour is controlled by a combination of FDs, providing energy dissipation capacity, and PT bars with disk springs, introducing restoring forces in the connection. The overall connection has dimensions comparable to the size of a traditional column splice. It is located above a traditional full-strength base plate joint, as illustrated in Figure 1(a). The FDs are composed of friction pads coated with thermally sprayed metal, pre-stressed with high strength bolts, placed between the steel cover plates and the column, as described in Figure 1(b). The disk springs, arranged in parallel and series, act as a macro-spring system, ensuring sufficient deformability to the connection and an adaptable stiffness-resistance combination. Figure 1(b) shows the details of the oversized and slotted holes of the column's web and flanges, which are designed to accommodate the gap opening required to reach the target rotation.

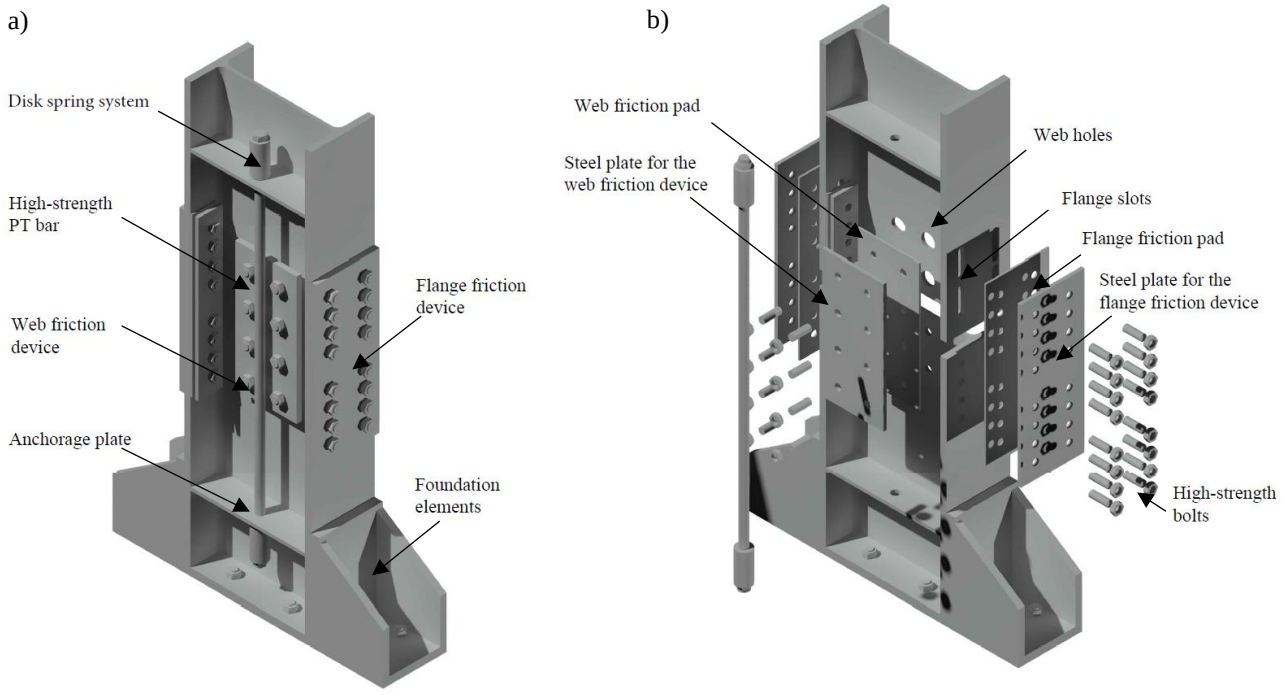

Figure 1. Self-centring column base connection: (a) 3D view; (b) 3D exploded view.

Considering this connection typology, Elettore *et al.* [51] recently investigated, through numerical simulations, the seismic response of a 4-storey – 3-bays MRF, which uses conventional beam-to-column joints and the SC-CB connections developed by Latour *et al.* [50]. The results show that the introduction of SC-CBs is an effective strategy to reduce the residual drifts of the whole frame and protect the first storey columns from yielding, with the additional benefit of limiting the number of self-centring devices.

Although several technologies for self-centring connections have been developed for both beam-to-column and CB joints, only a few research studies investigated the significant parameters (*e.g.*, properties of beam-to-column connections, properties of the CBs, frame layout) that influence the self-centring capability of these systems providing useful insights for the design. Moradi *et al.* [52] conducted a parametric analysis to study the influence of material and geometrical properties of PT beam-to-column connections (*i.e.*, beam depth, column height, and PT strand force) on the lateral response of these systems. Kamperidis *et al.* [53] investigated the effects of several specific local structural properties of the SC-CBs (*i.e.*, the initial stiffness, post-yield stiffness and strength of the CBs) on the seismic performance and collapse capacity of the benchmark frame. Moreover, Herning *et al.* [54] performed a reliability-based study to investigate the

sensitivity of SC-MRFs performances to some structural properties and geometry (*i.e.,* PT beam-to-column connection details). 3-,9- and 20- storey steel prototypes SC-MRFs have been investigated in order to propose improvements to the existing design procedure of these systems.

Within this context, the present paper performs a parametric analysis to investigate the frame layout's influence on the self-centring capability of perimeter MRFs with the SC-CB connections proposed in [50]. Nine case-studies buildings with a different number of storeys (*i.e.,* 4, 6 and 8) and bays (*i.e.,* 5, 7 and 9) have been designed according to the Eurocode 8 [1] and numerically investigated. State-of-the-art numerical models of the frames have been developed in OpenSees [55], with and without the investigated SC-CB connections. Incremental Dynamic Analyses (IDAs) [56] have been carried out considering a set of 30 ground motion records accounting for the influence of the uncertainty related to the earthquake input, *i.e.,* the record-to-record variability. The spectral acceleration corresponding to the fundamental period of vibration ($S_a(T_1,\xi)$) has been used as intensity measure (IM) while both global, and story-level engineering demand parameters (EDPs) have been monitored in order to compare the seismic performances of the frames. Fragility curves [57] have been successively developed, providing the probability of exceeding a residual interstorey drift limit equal to the 0.5%, conventionally associated with building reparability [33]. Results highlight that the efficiency of the SC-CBs in reducing the residual interstorey drifts is significantly affected by the number of storeys of the frames. In particular, the SC-CBs contributes to maximizing the self-centring capability at the lower storeys for all the structures, while its efficiency decreases along with the height. In addition, the introduction of the adopted connection does not provide detrimental effects in terms of peak interstorey drifts.

2 SELF-CENTRING DAMAGE-FREE COLUMN BASES

2.1 Moment-rotation behaviour

The column base connection experimentally tested by Latour *et al.* [50] and considered in this paper exhibits a moment-rotation hysteretic behaviour which can be easily calibrated. Figure 2(a) illustrates the expected forces of each component during the rocking behaviour: F_C represents the compression force at the centre of rotation (COR); F_w and F_f represent the sliding forces in the friction pads on the column web and flanges respectively; F_{PT} is the sum of the forces provided by the PT bars with disk springs. This force can be calculated by considering the sum of the initial post-tensioning forces $F_{PT,0}$, and the additional force consequent to the gap opening while rocking ΔF_{PT}. Additionally, N_{Ed}, M_{Ed} and V_{Ed} are the design actions (*i.e.,* axial force, bending moment and shear force) applied to the joint section, h_c is the height of the column section and t_{fc} is the thickness of the column flange.

The moment-rotation behaviour of the SC-CB is a function of the forces developed by each component and can be derived based on the static equilibrium at the COR during the rocking behaviour. The flag-shape moment-rotation hysteretic loop is illustrated in Figure 2(b) where: M_D is the decompression moment, *i.e.,* the sum of the moment contributions of the axial force M_N and the moment provided by the PT bars at zero rotation $M_{PT,0}$; M_{FD} is the moment provided by the FDs. M_1 is the moment that initiates the gap opening while M_2 is the maximum moment achieved at the design rotation $\theta_{joint,d}$ (*e.g.,* 0.04 rads as suggested by AISC 341-16 [3] for Special Moment Frames). The moments defining of the entire cyclic moment-rotation behaviour are given by:

$$M_D = \left(N_{Ed} + F_{PT,0}\right)\left(\frac{h_c - t_{fc}}{2}\right) \tag{1}$$

$$M_{FD} = F_f\,(h_c - t_{fc}) + 2F_w\left(\frac{h_c - t_{fc}}{2}\right) \tag{2}$$

$$M_1 = M_D + M_{FD} \tag{3}$$

$$M_2 = M_D + M_{FD} + K_{eq}\theta_{joint}\left(\frac{h_c - t_{fc}}{2}\right) \tag{4}$$

$$M_3 = M_2 - 2M_{FD} \tag{5}$$

$$M_4 = M_3 - M_{PT} \tag{6}$$

where K_{eq} is the equivalent axial stiffness of the system PT bars and disk springs [51].

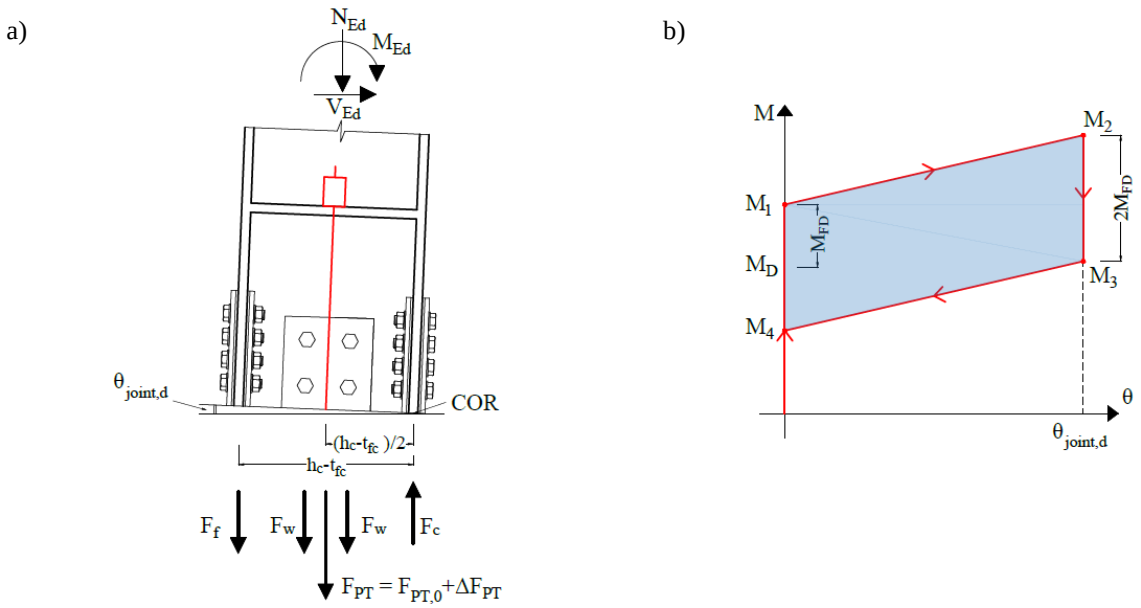

Figure 2. (a) Force interaction among the components during rocking; (b) Theoretical moment-rotation hysteretic curve.

2.2 Design of the components

The design of the proposed SC-CBs is based on the structural analysis of an 'equivalent' MRF with a fixed base. The axial design load N_{Ed} is derived from the amplified combination as required by Eurocode 8 [1], *i.e.*, $N_{Ed} = N_{Ed,G} + 1.1\gamma_{ov}\Omega N_{Ed,E}$, where: $N_{Ed,G}$ is the compression force due to the gravity loads of the seismic load combination; $N_{Ed,E}$ is the axial force due to the seismic design action; γ_{ov} is the overstrength factor equal to 1.25 while Ω is the minimum beam overstrength calculated as $\Omega_i = M_{pl,Rd,i}/M_{Ed,i}$, where $M_{Ed,i}$ is the design value of the bending moment in beam *i* in the seismic design situation and $M_{pl,Rd,i}$ is the corresponding plastic moment. The design moment M_{Ed} is calculated considering the amplified combination as required by Eurocode 8 [1], *i.e.*, $M_{Ed} = M_{Ed,G} + 1.1\gamma_{ov}\Omega M_{Ed,E}$, while the design shear force is assumed equal to $V_{Ed} = M_{Ed}/L_0$, where L_0 is the shear length.

Two main requirements must be satisfied during the design [51]: *1)* the maximum moment of the SC-CB, M_2, corresponding to the design rotation, $\theta_{joint,d}$, is lower than the yielding moment of the column $M_{pl,c}$ as reported in Eqn. (7); *2)* the self-centring behaviour of the connection is achieved if $M_4 > 0$. This condition is satisfied if the decompression moment M_D, is higher than the moment contribution of the FDs, M_{FD} as reported in Eqn. (8).

$$M_2 < M_{pl,c} \tag{7}$$

$$M_D \geq M_{FD} \rightarrow F_{PT} \geq 2F_f + 2F_w - N_{Ed} \tag{8}$$

It is worth highlighting that the moment-rotation behaviour is strongly affected by the axial force N_{Ed}. Hence, the above-mentioned checks must be performed by considering both the axial force's maximum and minimum values. In particular, the maximum (compressive) force represents the worst condition for the check required by Eqn. (7), while minimum (max tensile) force represents the worst condition for the check required by Eqn. (8). Based on these considerations, the initial sizing of the SC-CB is performed considering the max compressive axial force N_{Ed} for the inner columns where the variability of the axial force is limited. Conversely, for the external columns, where, due to the overturning moment, there is a significant variation of the axial force, the minimum (max tensile) force is considered for the design. Successively, the requirements of both Eqn.s (7) and (8) are checked for the other forces of each column.

The bolts in the web are preliminarily designed for the shear force $V_{Ed} = M_{Ed}/L_0$, and successively checked by considering the maximum moment developed by the connection (M_2), to ensure the capacity design against the shear mechanism. The bolts pre-load for the FD of the web is determined considering that the slippage force F_w is intended to resist the applied shear load as follows:

$$F_w = \mu \cdot n_{b,w} \cdot n_{s,w} \cdot F_{p,w} \geq V_{Ed} \tag{9}$$

where μ is the design value of the friction coefficient, $n_{b,w}$ is the number of bolts, $n_{s,w}$ is the number of friction interfaces (equal to two) and $F_{p,w}$ is the pre-load force of each bolt.

The post-tensioning force of the PT bars F_{PT} is obtained by imposing the system of equations for the self-centring condition of Eqn. (8) and the equilibrium between the internal and external moment in the CB as follow:

$$\begin{cases} F_{PT} \geq 2F_f + 2F_w - N_{Ed} \\ F_{PT} \cdot \left(\frac{h_c - t_{fc}}{2}\right) + F_f(h_c - t_{fc}) = M_{Ed} - (2F_w + N_{Ed})\left(\frac{h_c - t_{fc}}{2}\right) \end{cases} \quad (10)$$

where h_c and t_{fc} is the thickness of the column flange. Eqn.s (10) lead to the following simple design formulation:

$$F_{PT} \geq \frac{M_{Ed}}{(h_c - t_{fc})} - N_{Ed} \quad (11)$$

The following expression provides the pre-load for the FDs of the flanges:

$$F_f = \frac{M_{Ed}}{(h_c - t_{fc})} - \frac{1}{2}(2F_w + N_{Ed} + F_{PT}) \quad (12)$$

$$F_f = \mu \cdot n_{b,f} \cdot n_{s,f} \cdot F_{p,f} \quad (13)$$

where F_f is the slippage force of the FD of the flange, μ is the design value of the friction coefficient, $n_{b,f}$ is the number of bolts, $n_{s,f}$ is the number of friction interfaces (equal to two) and $F_{p,f}$ is the pre-load force of each bolt.

The disk springs system, obtained by disk springs arrangement in series and parallel, provides the ideal stiffness-resistance combination to the SC-CB. It is designed to be over-strength with respect to the PT bars by calibrating the number of the parallel disk springs. Conversely, the number of disks in series controls the system's stiffness, designed to avoid yielding the PT bars. The stiffness of the equivalent system K_{eq}, of the PT bars K_{PT} and of the disk spring system K_{ds} are defined as follows:

$$K_{eq} = \frac{K_{PT}K_{ds}}{K_{PT} + K_{ds}} \qquad K_{PT} = \frac{n_b E_{pt} A_{pt}}{l_{pt}} \qquad K_{ds} = \frac{n_{ds,par}}{n_{ds,ser}} K_{ds,1} \quad (14)$$

where n_b is the number of bars employed in the connection, l_{pt} is the bar length including the total length of the disk spring system (l_{ds}), $n_{ds,par}$ and $n_{ds,ser}$ are the number of disk springs in parallel and series respectively and $K_{ds,1}$ is the stiffness of the single disk spring. Finally, in order to allow the gap opening, the web holes and flange slots are designed to accommodate the design rotation $\theta_{joint,d}$. The holes' positions are designed complying with the edge distances and spacing of bolts suggested by Eurocode 3 [58].

3 CASE-STUDY FRAMES

3.1 Design of the case-study frames

Nine case-studies buildings with a different number of storeys (*i.e.*, 4, 6 and 8) and bays (*i.e.*, 5, 7 and 10) have been designed according to the Eurocode 8 [1] to investigates the influence of the frame layout on the seismic performance of perimeter MRFs with SC-CBs. The plan and the elevation views of the case-study frames are shown in Figure 3(a) and (b), respectively. The nine case-study buildings have 4, 6 and 8 storeys; 5, 7 and 10 bays in the *x*-direction and 3 bays in the *y*-direction. The horizontal resisting system is composed by perimeter MRFs, while the interior part is composed of gravity frames (*i.e.*, with 'pinned' beam-to-column connections and 'pinned' CBs). The layout has interstorey heights of 3.20 m except for the first level, whose height is equal to 3.50 m, while all the bays, in both directions, have spans of 6 m. The study investigates the seismic response of the MRFs in the *x*-direction having 3, 5 and 8 bays.

Two configurations are analysed and compared for each case-study: the first is the 'equivalent' MRF with conventional full-strength CBs, the second is the MRF including the SC-CB connections designed following the methodology presented in Section 2.

Uniform permanent load G_k = 4.5 kN/m^2 and uniform variable load q_k = 2.0 kN/m^2 have been assumed in the design. In addition, a uniform load for cladding of 2.0 kN/m is considered only for the external beams at the intermediate storeys. The seismic masses have been evaluated according to the seismic combination of the Eurocode 8 [1].

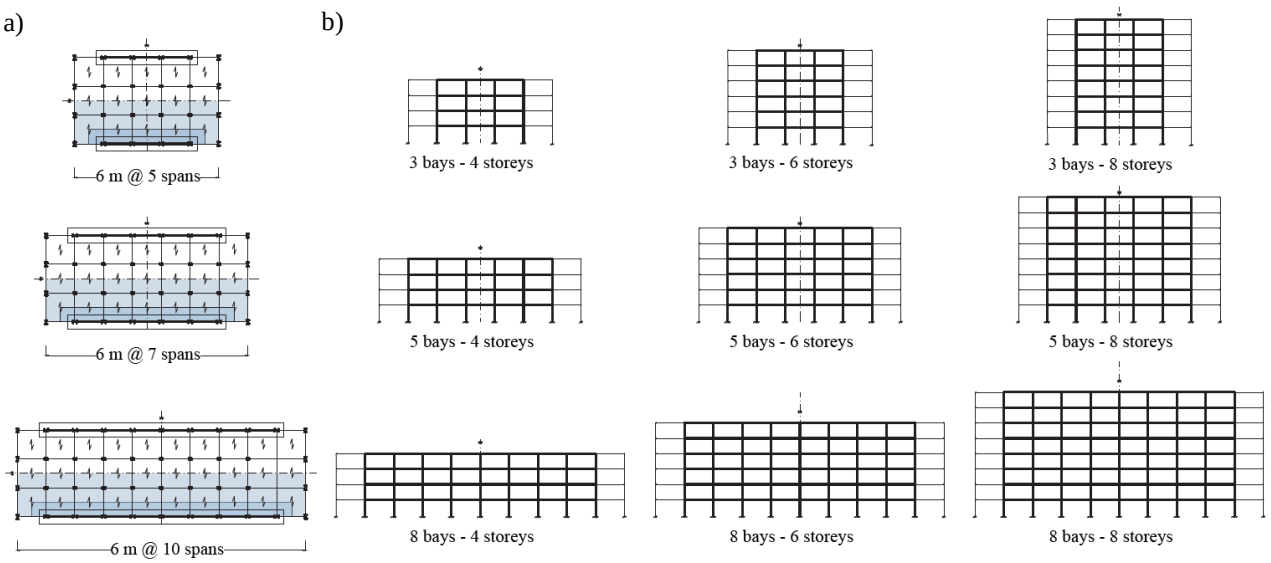

Figure 3. Case-study buildings: (a) Plan views; (b) Elevation views.

The Type-1 elastic response spectrum with a 2% damping factor ξ, a peak ground acceleration (PGA) equal to 0.35g, and soil type C is considered for the definition of the Design-Based Earthquake (*i.e.*, DBE, Ultimate Limit State according to the European definition) and is illustrated in

Figure 4. The behaviour factor used for the definition of the design spectrum is assumed equal to q = 6.5 in accordance with the requirements of the Eurocode 8 [1] for MRFs in DCH. The Maximum Credible Earthquake (*i.e.*, MCE, Collapse Limit State according to the European definition) is assumed to have an intensity equal to 150% the DBE.

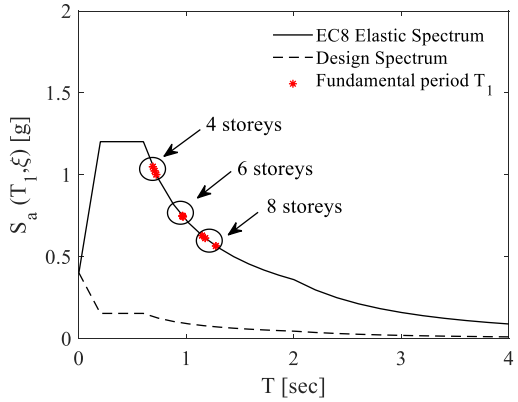

Figure 4. EC 8 Elastic and Design Spectra with indications of the periods of the frames.

Steel S275 (yielding stress f_y = 275 MPa) and S355 (f_y = 355 MPa) are used respectively for beams and columns. Beam-to-column connections are conventional full-strength rigid joints. The panel zones are stiffened with doubler plates with a thickness equal to the one of the column's web in order to ensure adequate strength to the joints hence promoting the plastic engagement of the beams only, in accordance with the capacity design rules. The floor is made by HI BOND A55/P600 type, hence ensuring the slab's rigid behaviour. The interstorey drift limit for the Damage State Limitation (DSL) requirements is assumed equal to 1% as suggested by Eurocode 8[1] for structures having non-structural elements fixed in a way so as not to interfere with structural deformations. Table 1 reports the profiles' cross-section for each of the designed case-study frames.

Table 2 reports the fundamental periods of vibrations and the spectral accelerations corresponding to both the DBE ($S_{a,DBE}$) and MCE ($S_{a,MCE}$), while Table 3 reports the distribution of the interstorey drifts evaluated at the DSL and the minimum overstrength factors (Ω_{min}), defined according to Eurocode 8 provisions [1]. It is important to highlight that the stiffness requirement related to the DSL is the one that controls the sizing of beams and columns and that the design of the frames has been performed by considering code prescriptions and technological requirements in a consistent way such that it allows assessing the influence of the design strategy on the seismic response of the different case-studies. The P-delta effects are not taken into account since the interstorey drift sensitivity coefficient θ is less than 0.1, at all the storeys of all the case-study frames, where θ is calculated following Eurocode 8 requirements [1].

Table 1. Profiles' cross-sections.

MRF 3-4			MRF 3-6			MRF 3-8		
Floor	Beams	Columns	Floor	Beams	Columns	Floor	Beams	Columns
						1	IPE 600	HE 650M
			1	IPE 600	HE 600M	2	IPE 600	HE 650M
1	IPE 550	HE 550M	2	IPE 600	HE 600M	3	IPE 600	HE 600M
2	IPE 550	HE 550M	3	IPE 600	HE 500M	4	IPE 600	HE 600M
3	IPE 550	HE 450M	4	IPE 600	HE 500M	5	IPE 550	HE 600M
4	IPE 550	HE 450M	5	IPE 550	HE 400M	6	IPE 550	HE 500M
			6	IPE 550	HE 400M	7	IPE 500	HE 500M
						8	IPE 500	HE 500M
MRF 5-4			MRF 5-6			MRF 5-8		
Floor	Beams	Columns	Floor	Beams	Columns	Floor	Beams	Columns
						1	IPE 600	HE 650M
			1	IPE 600	HE 500M	2	IPE 600	HE 650M
1	IPE 550	HE 450M	2	IPE 600	HE 500M	3	IPE 600	HE 600M
2	IPE 550	HE 450M	3	IPE 600	HE 400M	4	IPE 600	HE 600M
3	IPE 550	HE 360M	4	IPE 600	HE 400M	5	IPE 550	HE 600M
4	IPE 550	HE 360M	5	IPE 550	HE 340M	6	IPE 550	HE 500M
			6	IPE 550	HE 340M	7	IPE 500	HE 500M
						8	IPE 500	HE 500M
MRF 8-4			MRF 8-6			MRF 8-8		
Floor	Beams	Columns	Floor	Beams	Columns	Floor	Beams	Columns
						1	IPE 600	HE 600M
			1	IPE 600	HE 450M	2	IPE 600	HE 600M
1	IPE 550	HE 450M	2	IPE 600	HE 450M	3	IPE 600	HE 550M
2	IPE 550	HE 450M	3	IPE 600	HE 360M	4	IPE 600	HE 550M
3	IPE 550	HE 360M	4	IPE 600	HE 360M	5	IPE 550	HE 550M
4	IPE 550	HE 360M	5	IPE 550	HE 320M	6	IPE 550	HE 500M
			6	IPE 550	HE 320M	7	IPE 500	HE 500M
						8	IPE 500	HE 500M

Table 2. Fundamental Period (T_1) and spectral acceleration ($S_a(T_1,\xi)$) for DBE and MCE.

MRF 3-4			MRF 3-6			MRF 3-8		
T_1 [sec]	$S_{a,\,DBE}$ [g]	$S_{a,\,MCE}$ [g]	T_1 [sec]	$S_{a,\,DBE}$ [g]	$S_{a,\,MCE}$ [g]	T_1 [sec]	$S_{a,\,DBE}$ [g]	$S_{a,\,MCE}$ [g]
0.70	1.02	1.54	0.96	0.75	1.12	1.27	0.57	0.85
MRF 5-4			MRF 5-6			MRF 5-8		
T_1 [sec]	$S_{a,\,DBE}$ [g]	$S_{a,\,MCE}$ [g]	T_1 [sec]	$S_{a,\,DBE}$ [g]	$S_{a,\,MCE}$ [g]	T_1 [sec]	$S_{a,\,DBE}$ [g]	$S_{a,\,MCE}$ [g]
0.72	1.00	1.50	0.97	0.74	1.12	1.17	0.61	0.92
MRF 8-4			MRF 8-6			MRF 8-8		
T_1 [sec]	$S_{a,\,DBE}$ [g]	$S_{a,\,MCE}$ [g]	T_1 [sec]	$S_{a,\,DBE}$ [g]	$S_{a,\,MCE}$ [g]	T_1 [sec]	$S_{a,\,DBE}$ [g]	$S_{a,\,MCE}$ [g]
0.69	1.05	1.57	0.96	0.75	1.13	1.15	0.63	0.94

Table 3. Damage State Limitation (DSL) check and Ω_{min}.

MRF 3-4	MRF 3-6	MRF 3-8
Ω_{min} = 2.16	Ω_{min} = 2.14	Ω_{min} = 2.10
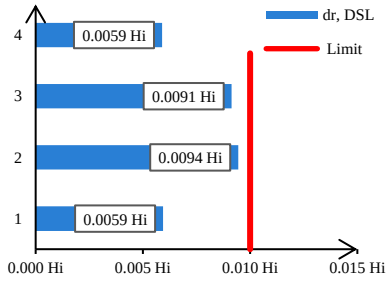	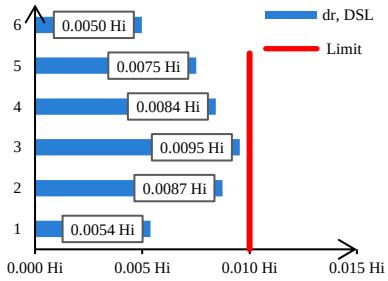	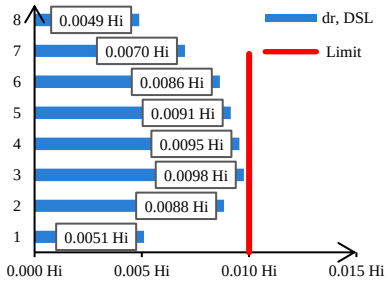
MRF 5-4	**MRF 5-6**	**MRF 5-8**
Ω_{min} = 2.18	Ω_{min} = 2.08	Ω_{min} = 2.03
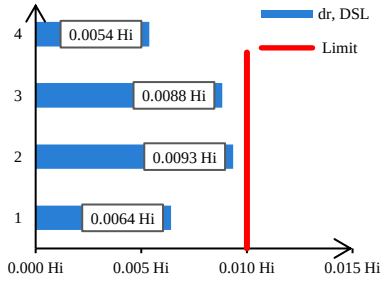	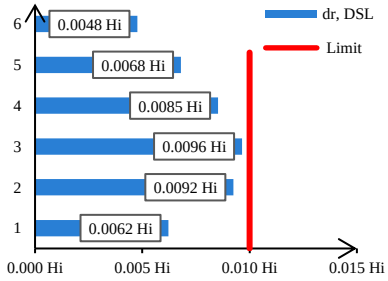	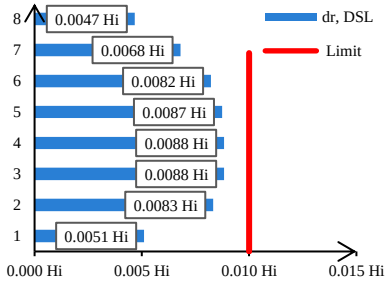
MRF 8-4	**MRF 8-6**	**MRF 8-8**
Ω_{min} = 2.25	Ω_{min} = 2.13	Ω_{min} = 2.12
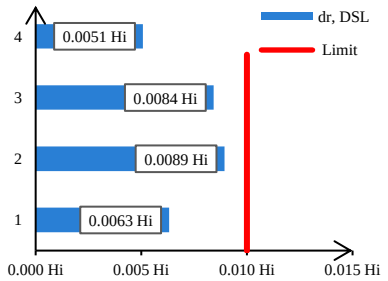	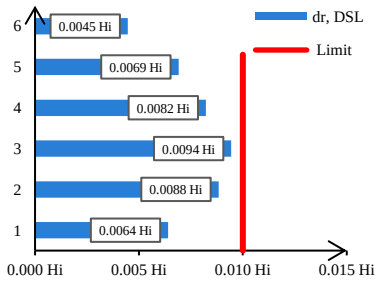	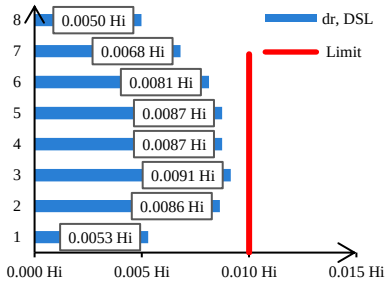

3.2 Design of the self-centring column base (SC-CB) connections

Once finalized the design of the frames with rigid full-strength CBs, the damage-free SC-CB connections are designed according to the procedure presented in Section 2. The design axial force N_{Ed} for the inner and outer columns of each case-study are reported in Table 4.

Table 4. Design axial forces.

MRF 3-4		MRF 3-6		MRF 3-8	
N_{Ed} [kN]		N_{Ed} [kN]		N_{Ed} [kN]	
Outer column	Inner column	Outer column	Inner column	Outer column	Inner column
+719	-451	+1318	-667	+1721	-812
MRF 5-4		**MRF 5-6**		**MRF 5-8**	
N_{Ed} [kN]		N_{Ed} [kN]		N_{Ed} [kN]	
Outer column	Inner column	Outer column	Inner column	Outer column	Inner column
+623	-550	+1133	-815	+1434	-933
MRF 8-4		**MRF 8-6**		**MRF 8-8**	
N_{Ed} [kN]		N_{Ed} [kN]		N_{Ed} [kN]	
Outer column	Inner column	Outer column	Inner column	Outer column	Inner column
+707	-574	+1023	-805	+1397	-952

Note: negative values are for compression; positive values are for tension.

With the design actions, FDs, PT bars and the disk spring system are designed accordingly. The friction pads are chosen according to the results of previous tests carried out by Cavallaro *et al.* [59-60], and consist of 8 mm of thermally

sprayed friction metal steel shims with friction coefficient equal to $\mu = 0.53$. The bolts for the FDs of web and flanges are HV M30 10.9 class, which are one of the most commonly used types of pre-loadable bolts and they are key components influencing strength, stiffness and ductility of the connections [61-62]. However, the influence of the bolts type on the structural behaviour of the CB connections is not considered in this study.

The PT bars are high-strength M36 with a maximum post-tensioning capacity of 514 kN, while the resistance and the stiffness (K_{ds1}) of each disk spring are 200 kN and 100 kN/mm, respectively. The material properties are summarised in Table 5 where E, f_y and f_u are the nominal values of the Young's modulus, the yield strength and ultimate tensile strength of the materials, respectively. The other proprieties of the adopted structural steel (*i.e.*, the shear modulus, the Poisson's ratio) are based on the Eurocode 3 [63]. Table 6 summarises the number and the pre-load for the bolts of the FDs and PT bars of the inner and outer columns. Table 7 reports the parameters of the moment-rotation behaviour for each SC-CB connection, *i.e.*, the decompression moment M_D, the moment corresponding to the gap-opening M_1 and the moment at the design rotation M_2.

Table 5. Material properties of the column base connections.

Elements	Class [-]	E [GPa]	f_y [MPa]	f_u [MPa]
Column and plates	S355	210	355	510
Post-tensioned bars	10.9	205	900	1000
Web Bolts	10.9	210	900	1000
Flange Bolts	10.9	210	900	1000

Table 6. Material properties.

		MRF 3-4		MRF 3-6		MRF 3-8	
		Outer column	Inner column	Outer column	Inner column	Outer column	Inner column
PT bars	Number [-]	8	6	8	6	8	4
Web bolts	Number [-]	4	4	4	4	4	4
	Pre-load [kN]	135	155	140	175	140	170
Flange bolts	Number [-]	8	8	8	8	8	8
	Pre-load [kN]	110	130	135	105	75	100
		MRF 5-4		MRF 5-6		MRF 5-8	
		Outer column	Inner column	Outer column	Inner column	Outer column	Inner column
PT bars	Number [-]	8	6	8	6	8	6
Web bolts	Number [-]	4	4	4	4	4	4
	Pre-load [kN]	120	125	130	165	135	170
Flange bolts	Number [-]	8	8	8	8	8	8
	Pre-load [kN]	105	120	120	100	135	80
		MRF 8-4		MRF 8-6		MRF 8-8	
		Outer column	Inner column	Outer column	Inner column	Outer column	Inner column
PT bars	Number [-]	8	6	8	6	8	6
Web bolts	Number [-]	4	4	4	4	4	4
	Pre-load [kN]	135	165	130	160	140	170
Flange bolts	Number [-]	8	8	8	8	8	8
	Pre-load [kN]	150	155	120	100	140	130

Table 7. Parameters of the moment-rotation behaviour.

	MRF 3-4		MRF 3-6		MRF 3-8	
	Outer column	Inner column	Outer column	Inner column	Outer column	Inner column
M_N [kNm]	(-)206	129	(-)409	207	(-)575	271
M_D [kNm]	1101	1109	1007	1269	951	1034
M_1 [kNm]	1779	1895	1883	2020	1557	1811
M_2 [kNm]	2120	2150	2104	2320	1852	2043
	MRF 5-4		MRF 5-6		MRF 5-8	
	Outer column	Inner column	Outer column	Inner column	Outer column	Inner column
M_N [kNm]	(-)149	131	(-)409	207	(-)479	311
M_D [kNm]	943	950	1007	1269	1047	1456
M_1 [kNm]	1472	1536	1883	2020	1980	2123
M_2 [kNm]	1650	1714	2104	2320	2275	2471
	MRF 8-4		MRF 8-6		MRF 8-8	
	Outer column	Inner column	Outer column	Inner column	Outer column	Inner column
M_N [kNm]	(-)169	137	(-)297	213	(-)433	295
M_D [kNm]	923	956	900	1111	983	1357
M_1 [kNm]	1642	1716	1557	1711	1879	2229
M_2 [kNm]	1859	1894	1771	1872	2133	2454

Note: the moments are calculated with the values of the axial design forces reported in Table 4. Consequently, for the columns in tensions M_N is opposite with respect to M_{PT}.

3.3 Frames and column base modelling

Two-dimensional finite element (FE) models of the frames with and without the SC-CB connection are developed in OpenSees [55] for all case-studies. The *'Steel01'* material [55] with 355 MPa and 275 MPa yield strengths and 0.2% post-yield stiffness ratio is used for columns and beams, respectively. Beams are modelled by a lumped plasticity approach where the plastic hinges are modelled as suggested by Lignos and Krawinkler [64]. Conversely, columns are modelled with a distributed plasticity approach with non-linear beam-column elements with four integration points. At beam-to-column connections, the *'Scissor'* model [65] simulates the panel zone stiffness and strength. Geometric non-linearities are considered in the elements of the MRF. In addition, a leaning column is included in the structural model to consider the P-Δ effects related to the gravity frames [66]. The rigid-floor diaphragm is modelled by assigning a high value to the axial stiffness to the beams. Gravity loads are applied on the beams by considering the seismic combination of the Eurocode 8 [1], while the masses are concentrated at the beam-to-column connections. Damping sources other than the hysteretic energy dissipation are modelled through Rayleigh damping where the values of the mass-related and stiffness-related damping coefficients are considered for a damping factor of 2% for the first two vibration modes.

The SC-CB connections are implemented by following the modelling strategy proposed by Elettore *et al.* [51]. The model is shown in Figure 5. The rocking interface's rigid elements are modelled with elastic elements [55] with very high flexural stiffness. These are connected to four non-linear springs represented by zero-length elements in parallel with gap elements simulating the bilinear hysteretic response of the FDs and the contact behaviour of the column interfaces FDs are modelled by the *'Steel01'* material [55] considering a very high initial stiffness and very low post-elastic stiffness, while the contacts elements are defined by the *'Elastic compression-no tension'* (ENT) material [55] with very high compression stiffness to model the contact behaviour. A central zero-length translational spring with bilinear elastic-plastic behaviour is used to model the system of PT bars and disk springs. The initial post-tensioning force of the PT bars is modelled by imposing an initial strain equal to $F_{PT}/A_{PT}E_{PT}$ by using the *'Initial strain material'* [55].

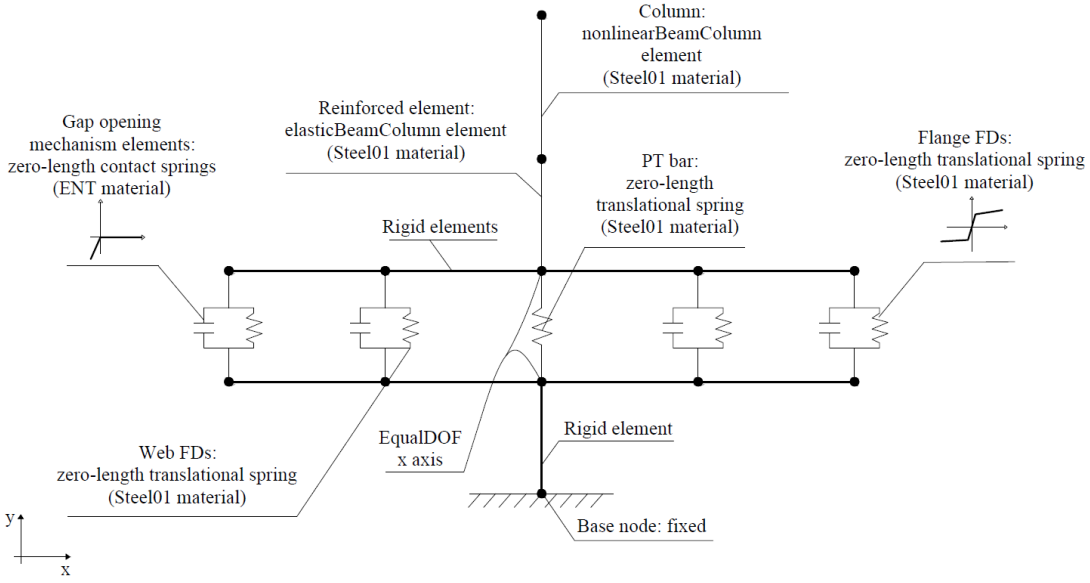

Figure 5. Two-dimensional column base model in OpenSees [55]

4 PERFORMANCE-BASED ASSESSMENT OF THE CASE-STUDY FRAMES

4.1 Ground motion selection

Incremental Dynamic Analyses (IDA) [56] have been carried out to investigate the seismic performances of the nine case-study frames in both configurations (*i.e.*, with and without the SC-CB connections). A suite of 30 ground motion records is selected from the SIMBAD Database using REXEL [67] accounting for the record-to-record variability. The set of ground motions is selected for each case-study with the following parameters: moment magnitude (M_w) ranging from 6 to 7, epicentral distance $R \leq 30$ km and spectrum-compatibility in the range of periods between $0.2T_1$ and $2T_1$, where T_1 is the fundamental period of the structure. The mean elastic spectrum of the records is kept between 75% and 130% of the corresponding Eurocode 8 based elastic response spectrum [1] considered for the design. It is noteworthy that a large number of zero acceleration points (*i.e.*, 40 s) have been added at the end of each record to allow the free vibrations to stop and correctly capture the residual deformations.

Within the IDA procedure, the ground motion records are scaled to increasing IM values with a constant step of 0.1g until 'collapse'. The spectral acceleration corresponding to the first vibration mode ($S_a(T_1,\xi)$) is used as IM. It is important to highlight that the vibration periods, and consequently the IM values, are the same for the two 'equivalent' structures with and without the SC-CBs hence allowing the comparison of fragility curves.

4.2 Incremental Dynamic Analysis

Global and storey-level EDPs are monitored to investigate the influence of the frame layout on the effectiveness of the proposed SC-CBs. Peak and residual interstorey drifts are considered story-level EDPs, while the maximum values of these quantities among all the storeys are used as global EDPs. The effectiveness of the SC-CBs in reducing the residual interstorey drifts is evaluated by the comparison between 'equivalent' MRF with conventional full-strength CBs and the MRF with SC-CB connections (MRF-CB). In the present study, residual interstorey drifts limit is assumed equal to 0.5 %, which is the conventional threshold beyond which repairing may not be economically viable [33].

Results are illustrated in Figure 6 only for a single case-study (*i.e.*, the 5-bays 6-storey frame in both configurations) to show the selected global EDPs monitored by the IDAs. Figure 6(a) and (b) show the IDA curves for the maximum (among all the storeys) peak interstorey drifts ($\theta_{max\text{-}peak}$), for the case-study frames having 5 bays and 6 storeys in both configurations. Similarly, Figure 6(c) and (d) show the IDA curves for the maximum (among all the storeys) residual interstorey drifts ($\theta_{max\text{-}res}$). Highlighted in the figures are the 16%, 50%, and 84% fractiles among all ground motions as a synthesis of the demand values for both quantities while the single IDA curves are shown in grey. The selected fractiles' values are reported for both seismic intensities of interest, DBE and MCE. The results in terms of $\theta_{max\text{-}res}$ for the other case-studies are shown in the Appendix. Conversely, the results of $\theta_{max\text{-}peak}$ for the other case-studies are not reported for the sake of brevity.

The comparison of Figure 6(a) and (b) shows that the introduction of SC-CBs does not alter the structures' maximum response. The selected fractiles of the maximum peak interstorey drift for the two configurations show similar values along with the whole range of IM intensities. Conversely, the comparison of Figure 6(c) and (d) shows that the use of the SC-CBs allows a significant reduction of the maximum residual interstorey drifts. In particular, Figure 6(d) shows that, considering the median results (50% fractile curve) among all ground motions, the introduction of the SC-CB allows a reduction of the residual interstorey drifts which is lower than the limit of 0.5% [33], for both the DBE and the MCE. Conversely, this limit is not satisfied for the MRF with conventional column bases at the MCE intensity.

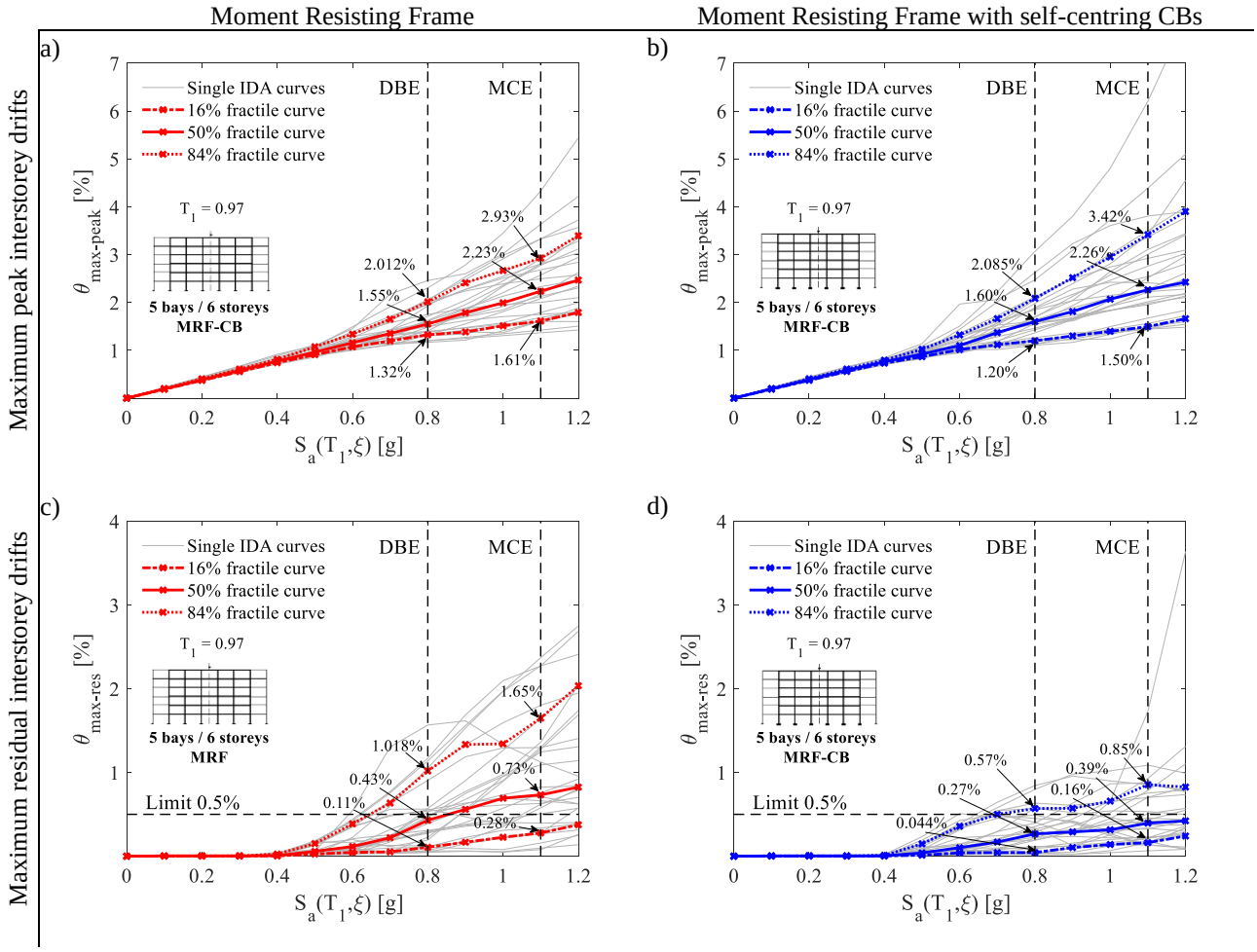

Figure 6. IDA Results: Maximum peak interstorey drifts: (a) MRF 5-6; (b) MRF-CB 5-6; Maximum residual interstorey drifts: (c) MRF 5-6; (d) MRF-CB 5-6

Figure 7 shows the comparison of the maximum residual interstorey drifts, synthesized by the median values ($\theta_{max\text{-}res,50\%}$), for all the considered structures (*i.e.*, with and without SC-CBs). The median values correspond to the 50% fractiles previously illustrated for the single case-study in Figure 6. Additionally, the percentage reduction (Δ) of the aforementioned parameter is reported for the two seismic intensities of interest. The figure highlights that the use of the SC-CBs allows for a significant reduction of the maximum residual interstorey drifts for all structures for both the DBE and the MCE. The only exception is related to the 8-storey frames, where the percentage reduction is limited at the DBE (*i.e.*, from 0% to 13%). However, it is noteworthy that all the structures equipped with the SC-CBs experience values of $\theta_{max\text{-}res,50\%}$ lower than the limit of the 0.5%, also when the 'equivalent' conventional MRFs overcome it. The comparison of these reduction values provides an understanding of the frame layout's influence on the effectiveness of the proposed SC-CBs in terms of residual drifts reduction.

In particular, the results show a high sensitivity of the self-centring response to the number of storeys of the structures. This is evidenced by the percentage reductions Δ observed in Figure 7(a), (b) and (c) of the 3-bays 4-storey, 3-bays 6-storey and 3-bays 8-storey frames, which assume decreasing values at the MCE (*i.e.*, from 70% to 36%). A similar trend can be seen for the 5-bays (*i.e.*, from 66% to 36%) and the 8-bays frames (*i.e.*, from 72% to 41%), at the same intensity, as shown in Figure 7(d), (e) and (f) and Figure 7(g), (h) and (i), respectively. It is highlighted that these results are particularly relevant at the MCE, due to the high plastic engagement of the plastic hinges of the structures.

Conversely, with respect to the number of bays, the frames' response does not show a clear tendency. In fact, it is not possible to observe a significant influence of the number of bays in reducing the efficiency of the SC-CBs, as evidenced in Figure 7(a), (d) and (g) by the values of the percentage reductions Δ of the 3-bays 4-storey, 5-bays 4-storey and 8-bays 4-storey frames, which experience similar values at the MCE (*i.e.*, from 66% to 72%). Similarly, this also occurs for the 6-storey (*i.e.*, from 42% to 54%) and the 8-storey frames (*i.e.*, from 36% to 41%) at the same intensity, as shown in Figure 7(b), (e) and (h) and Figure 7 (c), (f) and (i), respectively. Moreover, it is not possible to see a consistent trend at the DBE intensity.

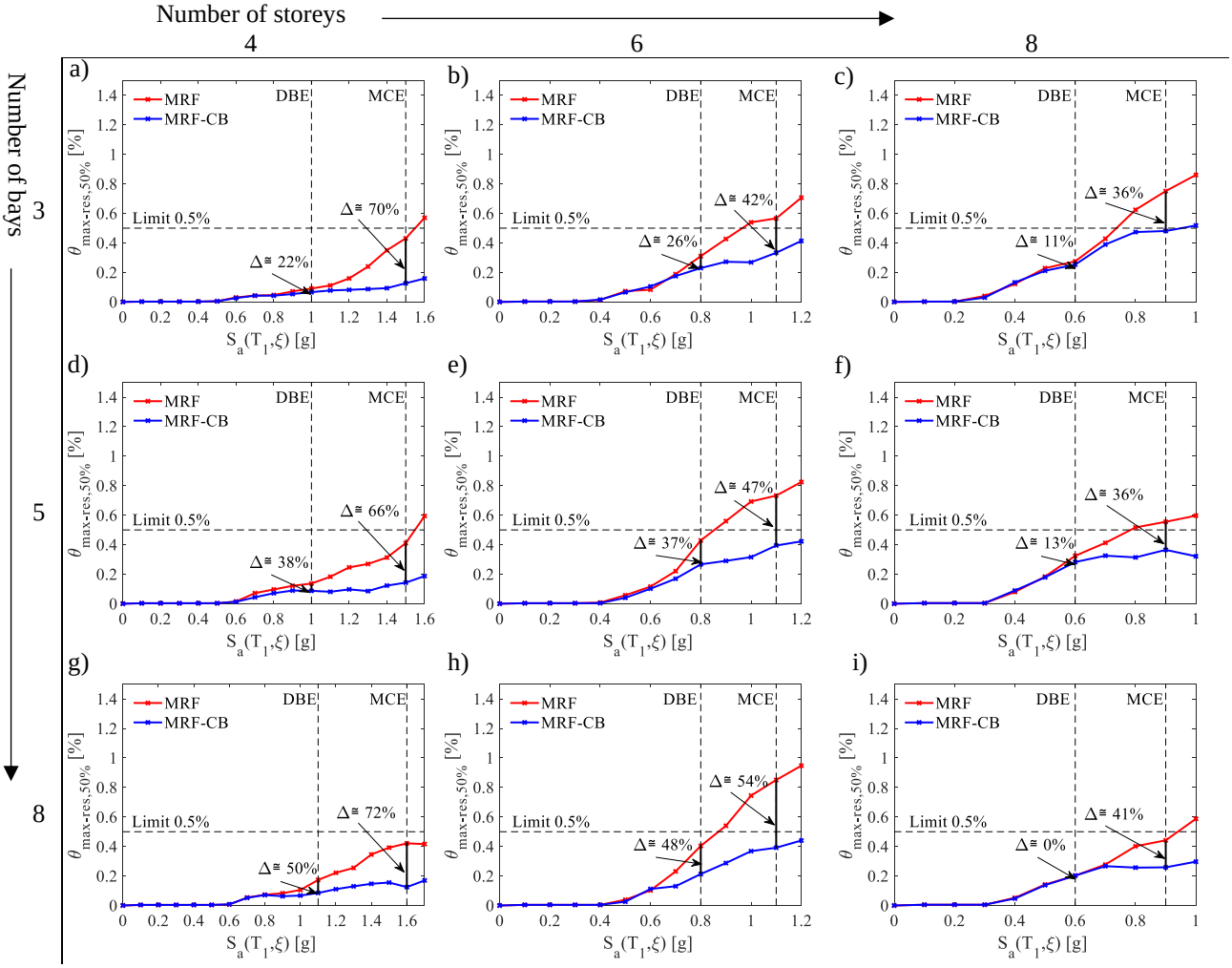

Figure 7. IDA Results: Comparison of the maximum residual interstorey drifts in terms of median values (50% fractile) among all ground motions: (a) 3-4; (b) 3-6; (c) 3-8; (d) 5-4; (e) 5-6; (f) 5-8; (g) 8-4; (h) 8-6; (i) 8-8.

In order to provide additional information about the trends of the selected EDPs at all the storeys of the case-studies in both configurations, the height-wise peak and residual interstorey drifts distributions are shown in Figure 8 and Figure 9, respectively.

Figure 8 illustrates the comparison of the peak interstorey drifts' distributions, synthesized by the median value ($\theta_{peak,50\%}$), for all the structures with and without the SC-CBs, at the MCE. As expected, based on the results shown in Figure 6(a) and (b), the 'equivalent' structures (*i.e.*, MRF and MRF-CB), are characterized by similar values and distribution for the peak interstorey drifts. The only exception is related to the first storeys where the structures equipped with SC-CBs show a slight increase in the peak interstorey drifts. This is expected and related to the lower effective (*i.e.*, tangent) stiffness of the SC-CB connection.

It is worth mentioning that for the 8-storey frames the maximum values of the peak interstorey drifts tend to concentrate at intermediate storeys. This highlights the influence of the higher modes in the response of these structures. Conversely, for the 4- and 6-storey frames, $\theta_{peak,50\%}$ assumes its maximum value at the lower storeys.

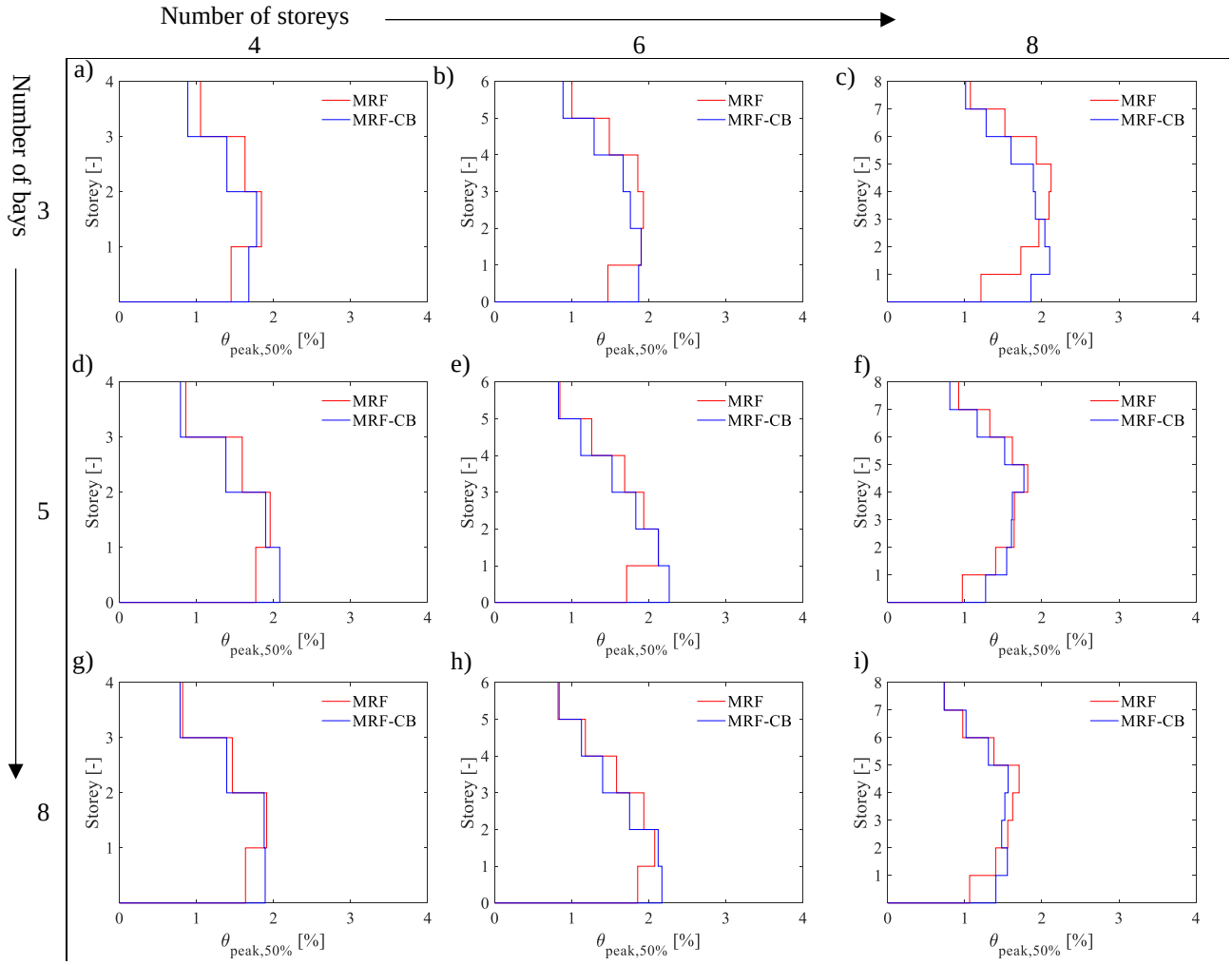

Figure 8. IDA Results: Comparison of the distribution of the peak storey drifts of the case-study frames for MCE: (a) 3-4; (b) 3-6; (c) 3-8; (d) 5-4; (e) 5-6; (f) 5-8; (g) 8-4; (h) 8-6; (i) 8-8.

Figure 9 shows the comparison of the residual interstorey drifts' distributions synthesized by the median value ($\theta_{res,50\%}$), for all the structures with and without the SC-CBs, at the MCE. The distribution patterns of the $\theta_{res,50\%}$ for the MRFs with conventional CBs are similar to the height-wise peak interstorey drifts distributions previously observed in Figure 8. In fact, the 4- and 6- storey conventional MRFs experience the maximum values of residual interstorey drifts at the first storeys, with a distribution pattern which is proportionally decreasing with the height. Conversely, for 8 storeys frames, the highest values of residual interstorey drifts occur at the intermediate storeys.

Differently, for the structures with SC-CBs it can be observed a significant reduction of the residual interstorey drifts in the lower storeys, while its effectiveness reduces and tends to disappear at higher storeys. For example, for the 5-bay 6-storey frames the value of $\theta_{res,50\%}$ is reduced of 83% (*i.e.*, from 0.71% to 0.12%) at the first storey, of 55% (*i.e.*, from 0.55% to 0.25%) at the third storey and of 41% (*i.e.*, from 0.083% to 0.049%) at the sixth storey. Similar trends can be seen for the other case-studies.

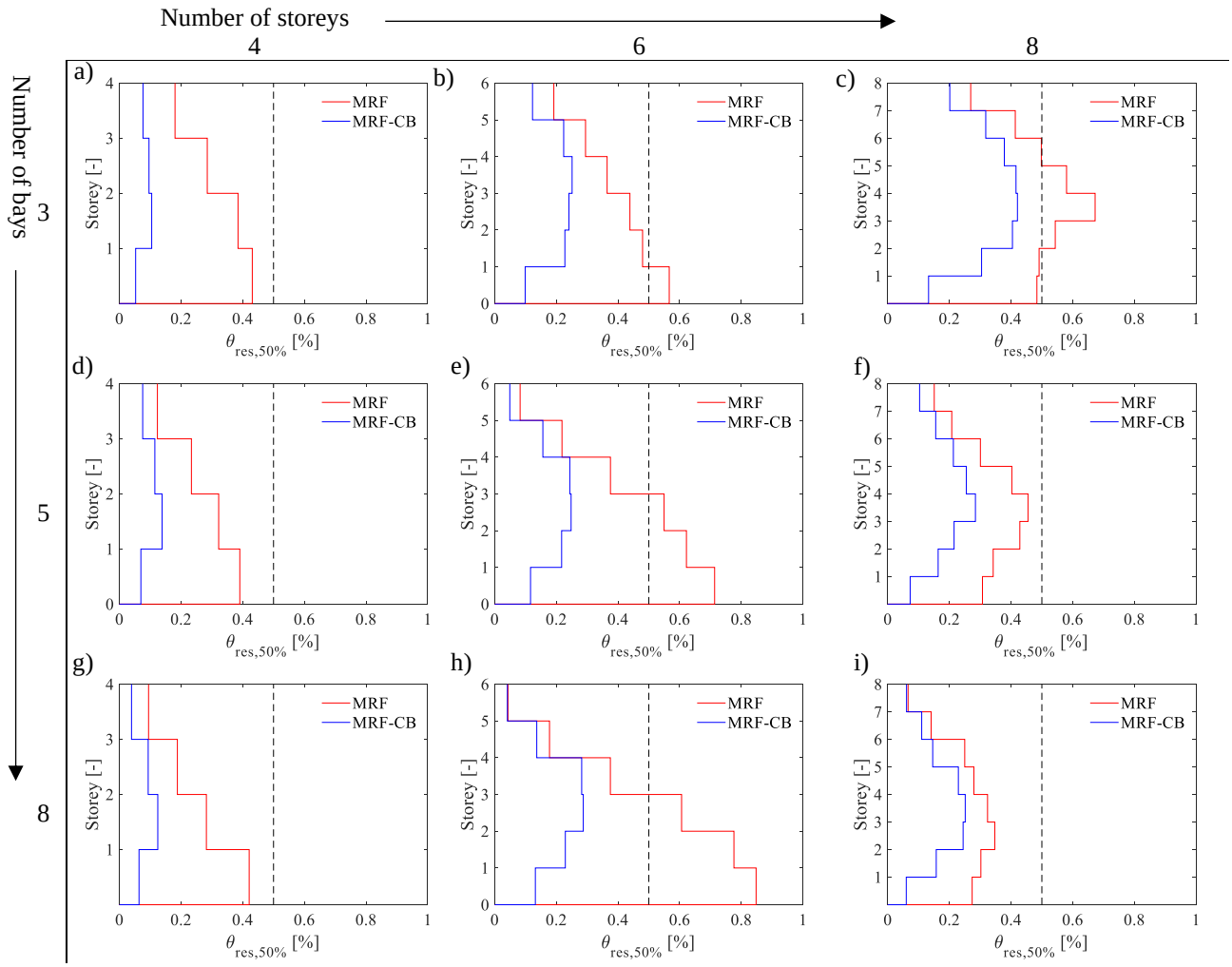

Figure 9. IDA Results: Comparison of the distribution of the residual storey drifts in terms of median values (50% fractile) among all ground motions of the case-study frames for MCE: (a) 3-4; (b) 3-6; (c) 3-8; (d) 5-4; (e) 5-6; (f) 5-8; (g) 8-4; (h) 8-6; (i) 8-8

4.3 Fragility Curves

Fragility curves are used in order to quantify the probability of the seismic demand exceeding an associated capacity threshold, given the seismic intensity, which is characterized by the IMs [68]. The spectral acceleration corresponding to the first vibration period (*i.e.*, $S_a(T_1,\xi)$) is assumed as IM. Global and storey-level residual response parameters (*i.e.*, the maximum residual interstorey drifts and the storey-level residual interstorey drifts) are considered as EDPs in order to investigate the self-centring capability of the structure. These values are compared with the associated capacity threshold which is conventionally assumed as 0.5% [33]. Numerical fragility curves are initially derived based on EDPs-IMs pairs obtained by the IDAs and successively fitted by analytical lognormal curves trough least-square minimization.

Such fragility curves provide the probability of exceeding the assumed residual interstorey drifts capacity value (*i.e.*, probability of failure P_f) vs the seismic IM values, giving insights on the self-centring capability, and hence the reparability of the structures. It is noteworthy that the fragilities provide a probabilistic interpretation of the results and of the sensitivity of the seismic response with respect to the frame layout. In this study, storey-level (*i.e.*, residual interstorey drifts as EDPs) and global fragility curves (*i.e.*, maximum residual interstorey drifts among all the storeys as EDPs) are derived.

The comparison of the global fragility curves is shown in Figure 10 for all the case-studies for the two configurations (*i.e.*, with and without the SC-CBs). The maximum (among all the storeys) residual interstorey drifts ($\theta_{max\text{-}res}$) is used as EDPs. Additionally, the percentage reductions of the probability of exceeding the limit value (*i.e.*, ΔP_f) are also reported for the two seismic intensities of interest (*i.e.*, DBE and MCE).

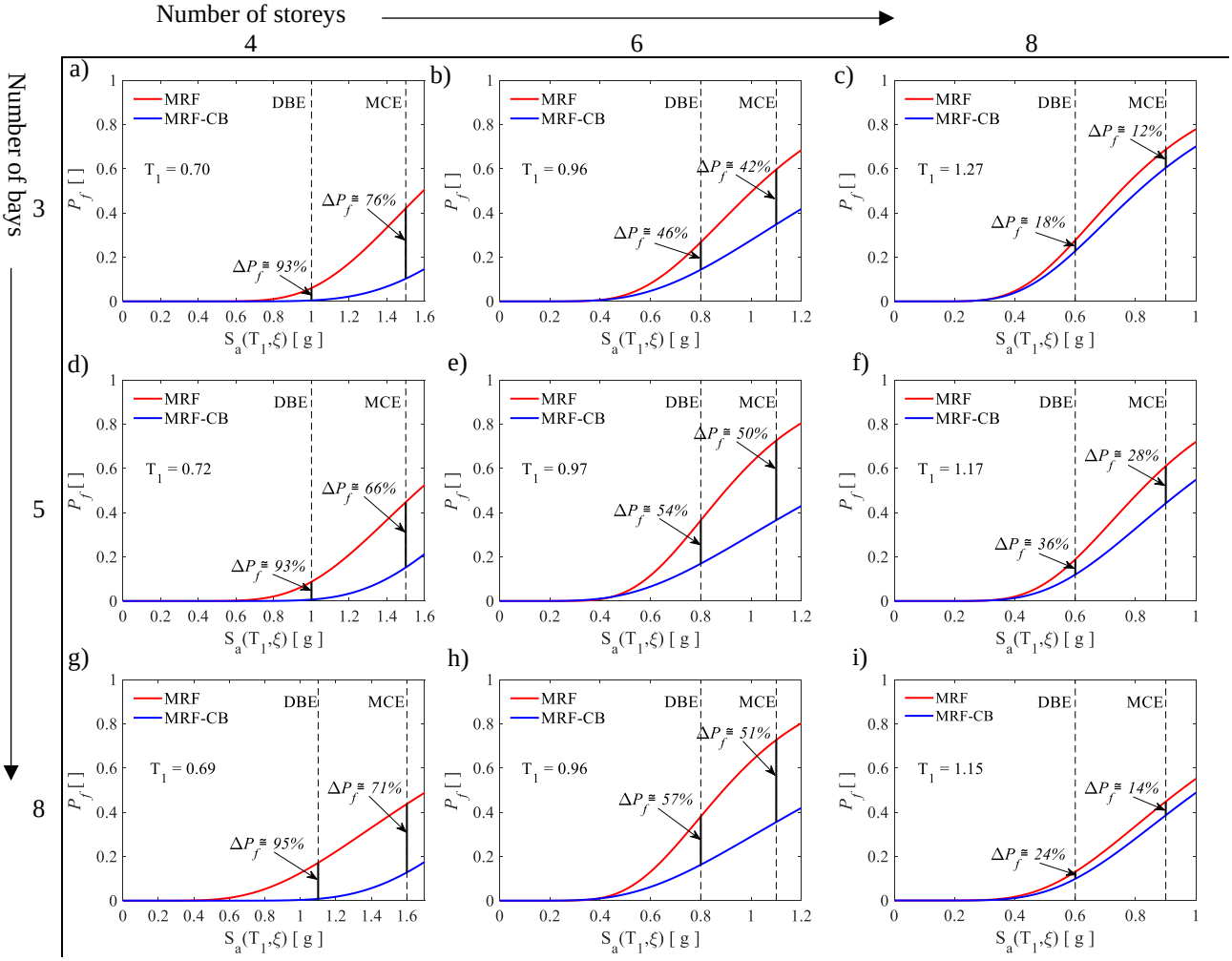

Figure 10. Comparison of the global fragility curves for the maximum residual interstorey drifts with respect to the threshold limit of 0.5%, for the case study frames: (a) 3-4; (b) 3-6; (c) 3-8; (d) 5-4; (e) 5-6; (f) 5-8; (g) 8-4; (h) 8-6; (i) 8-8.

Figure 10 provides, in a probabilistic framework, the results of the IDAs previously showed in Figure 6. In Figure 10 it is possible to point out a clear correlation between P_f and the increasing number of storeys, for both the DBE and the MCE. This is evidenced by the percentage reductions ΔP_f reported in Figure 10(a) (b) and (c) of the 3-bays 4-storey, 3-bays 6-storey and 3-bays 8-storey frames, which assume decreasing values at the DBE (*i.e.*, from 93% to 18%) and at the MCE (*i.e.*, from 76% to 12%). Similar behaviour is observed for the 5-bays and 8-bays frames. These results evidence that the ΔP_f decreases with the increasing height of the case-studies.

On the other hand, it is not possible to observe a significant sensitivity to the variation of the number of bays on the ΔP_f in all the structures, as highlighted in Figure 10(a) (d) and (g) by the ΔP_f of the 3-bays 4-storey, 5-bays 4-storey and 8-bays 4-storey frames, which experience similar values at the DBE (*i.e.*, from 93% to 95%) and at the MCE (*i.e.*, from 66% to 76%). A similar trend can be seen for the 5-storey and the 8-storey frames.

Furthermore, storey-level fragility curves are carried out to evaluate the probability of exceeding the threshold limit of 0.5% at each storey, for each case-study. Figure 11 shows the comparison of the fragility curves for each storey of all the case-study frames for the two configurations (*i.e.*, with and without the SC-CBs). The residual interstorey drifts are used as storey-level EDPs. The colour filled areas represent the interval between the most and the least fragile storeys (*i.e.*, red for the frames with conventional CBs, blue for the frames equipped with the SC-CBs).

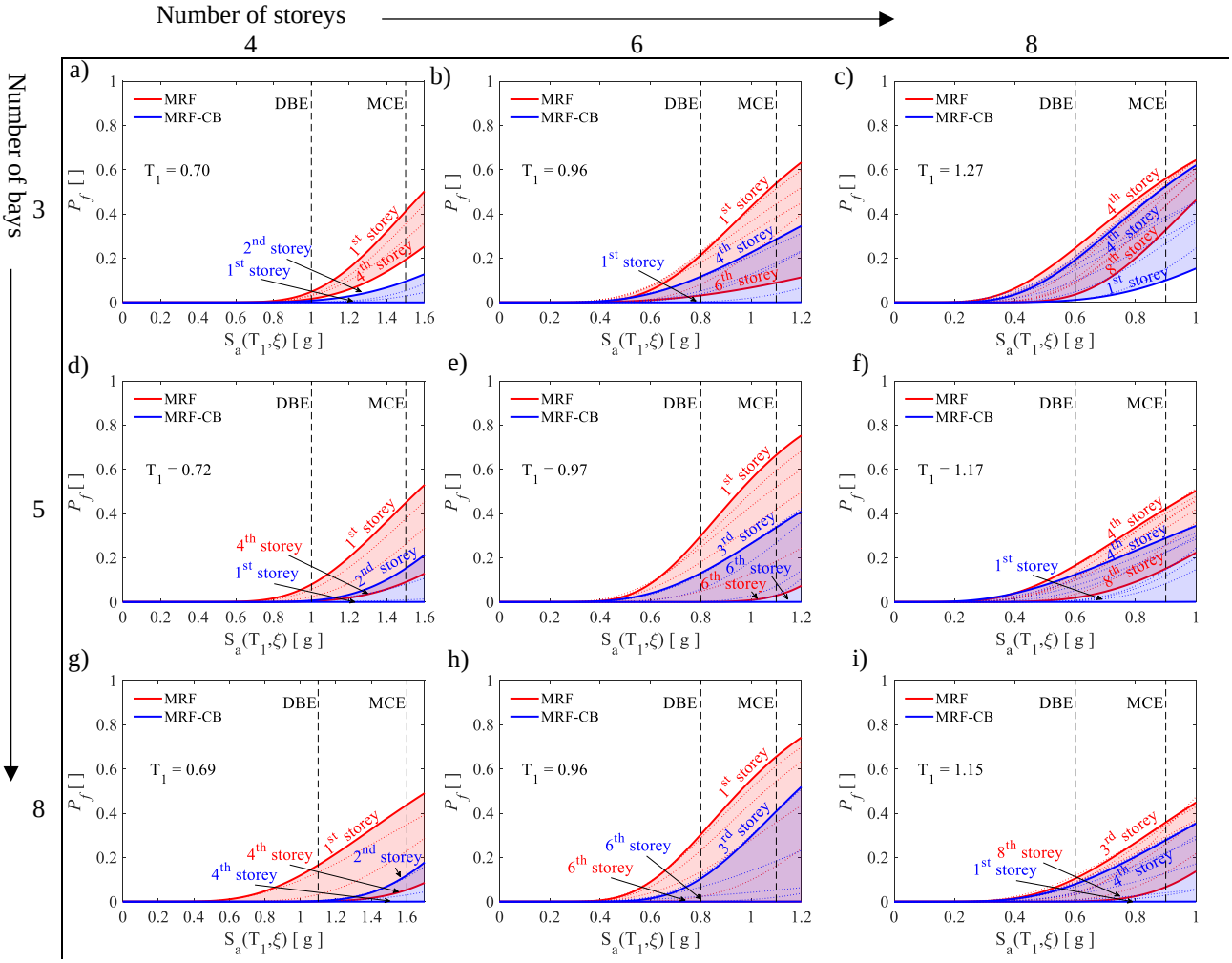

Figure 11. Comparison of the storey-level fragility curves for the residual interstorey drifts with respect to the threshold limit of 0.5%, for the case study frames: (a) 3-4; (b) 3-6; (c) 3-8; (d) 5-4; (e) 5-6; (f) 5-8; (g) 8-4; (h) 8-6; (i) 8-8.

In Figure 11 it is possible to observe a correlation with the height-wise distributions showed in Figure 9, in probabilistic terms. Figure 11 shows that, for all the structures equipped with conventional CBs, P_f is maximum at the 1st storey. The only exceptions are related to the 8-storey frames, where P_f is higher at the intermediate storeys (*i.e.*, 3rd – 4th storey), due to the influence of the higher modes. Conversely, P_f assumes the minimum values at the upper storeys. This behaviour highlights that the higher storeys of the structures experience smaller post-elastic deformations, as a consequence of the technological and design criteria adopted [1].

Regarding the structures equipped with the SC-CBs, the introduction of the proposed connections minimizes the probability of exceeding the 0.5% limit at the 1st storey (*i.e.*, $P_f \cong 0$). In some cases (*i.e.*, 8 bays 4 storey, 5 bays 6 storey and 8 bays 6 storey frames), due to the almost-elastic behaviour of the beams at the last storeys, the P_f of the last storeys assumes similar values to P_f at the 1st storey. Conversely, P_f is maximum at the intermediate storeys. These results demonstrate how the adoption of the SC-CBs provides a significant reduction of P_f at the lower storeys, while this effectiveness decreases along with the height, resulting in a reduction of the self-centring capability.

5 CONCLUSIONS

This study performs a parametric analysis with the aim of investigating the influence of the frame layout on the self-centring capability of perimeter steel Moment Resisting Frames equipped with damage-free self-centring column base connections, previously proposed by the authors. Nine case-study frames with a different number of storeys (*i.e.*, 4, 6 and 8) and bays (*i.e.*, 3, 5 and 8) have been designed and numerically investigated in OpenSees. Each case-study is examined in two configurations (*i.e.*, with and without the damage-free self-centring column bases). Incremental Dynamic Analyses are performed with a set of 30 ground motion records, assessing both global and storey-level engineering demand parameter, while accounting for the record-to-record variability. Fragility curves are derived to evaluate the self-centring

capability of the structures. The following conclusions can be drawn: 1) The seismic performances of the structures equipped with damage-free self-centring column base connections are significantly enhanced, as demonstrated by the significant residual drift reductions, at both the design based and maximum credible earthquake; 2) The self-centring capability of the adopted connections in reducing the residual interstorey drifts is particularly influenced by the number of storeys of the structures. Results show that the efficiency is relevant for the 4- and 6- storey frames, while it decreases for the 8-storey frames. Conversely, no sensitivity to the variation of the number of bays of the structures is observed; 3) The peak responses of the frames are not altered by the adoption of the damage-free self-centring column bases. In fact, the two configurations examined experience a similar height-wise distribution of the peak interstorey drifts; 4) The effectiveness of the adopted connection in reducing the residual interstorey drifts is relevant at the lower storeys, while it reduces at higher storeys, resulting in a reduction of the self-centring capability as evidenced by the 8- storey frames.

APPENDIX

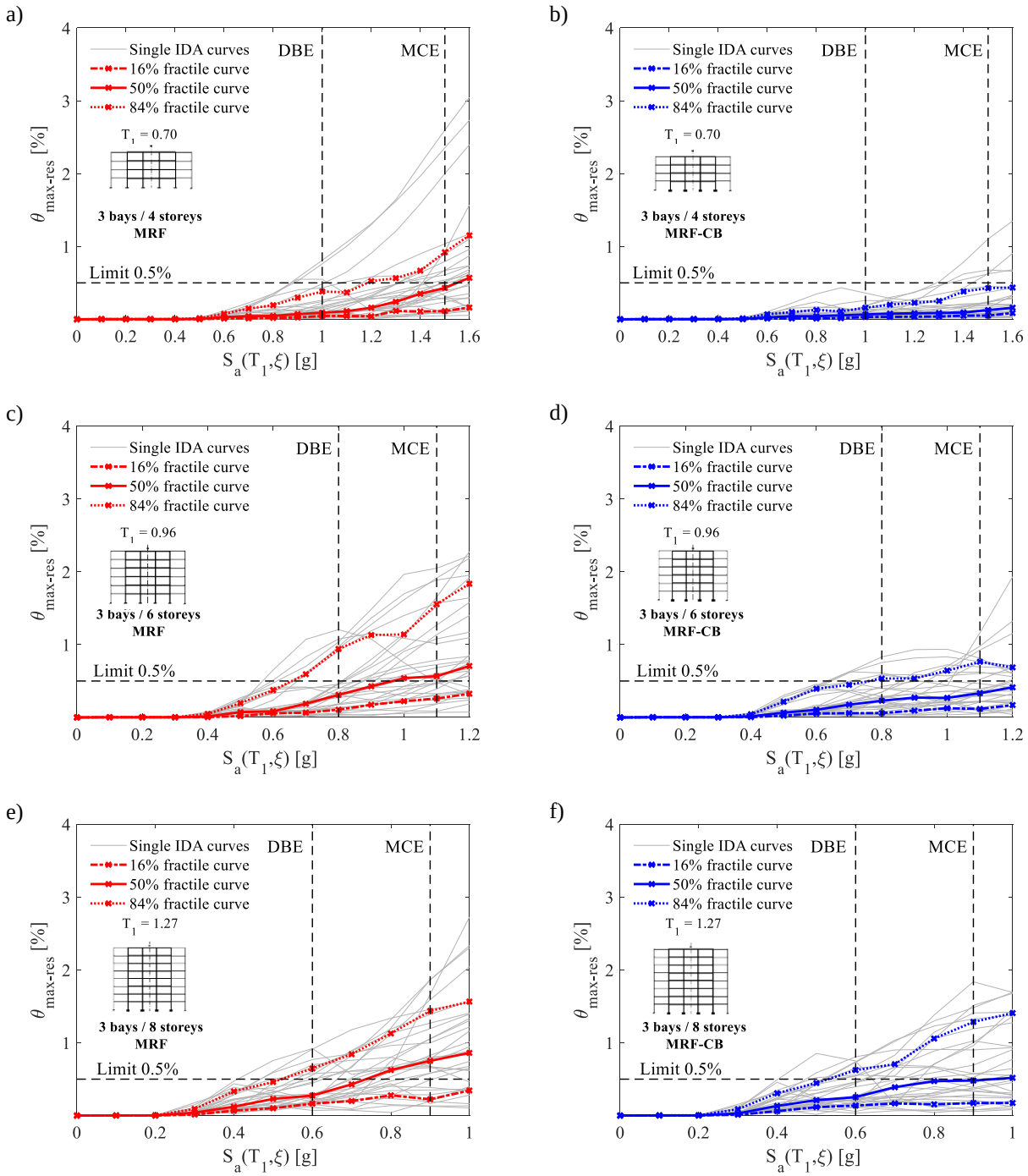

Figure A.1. IDA Results: Maximum residual interstorey drifts of the case-study frames: (a, b) 3-4; (c, d) 3-6; (e, f) 3-8.

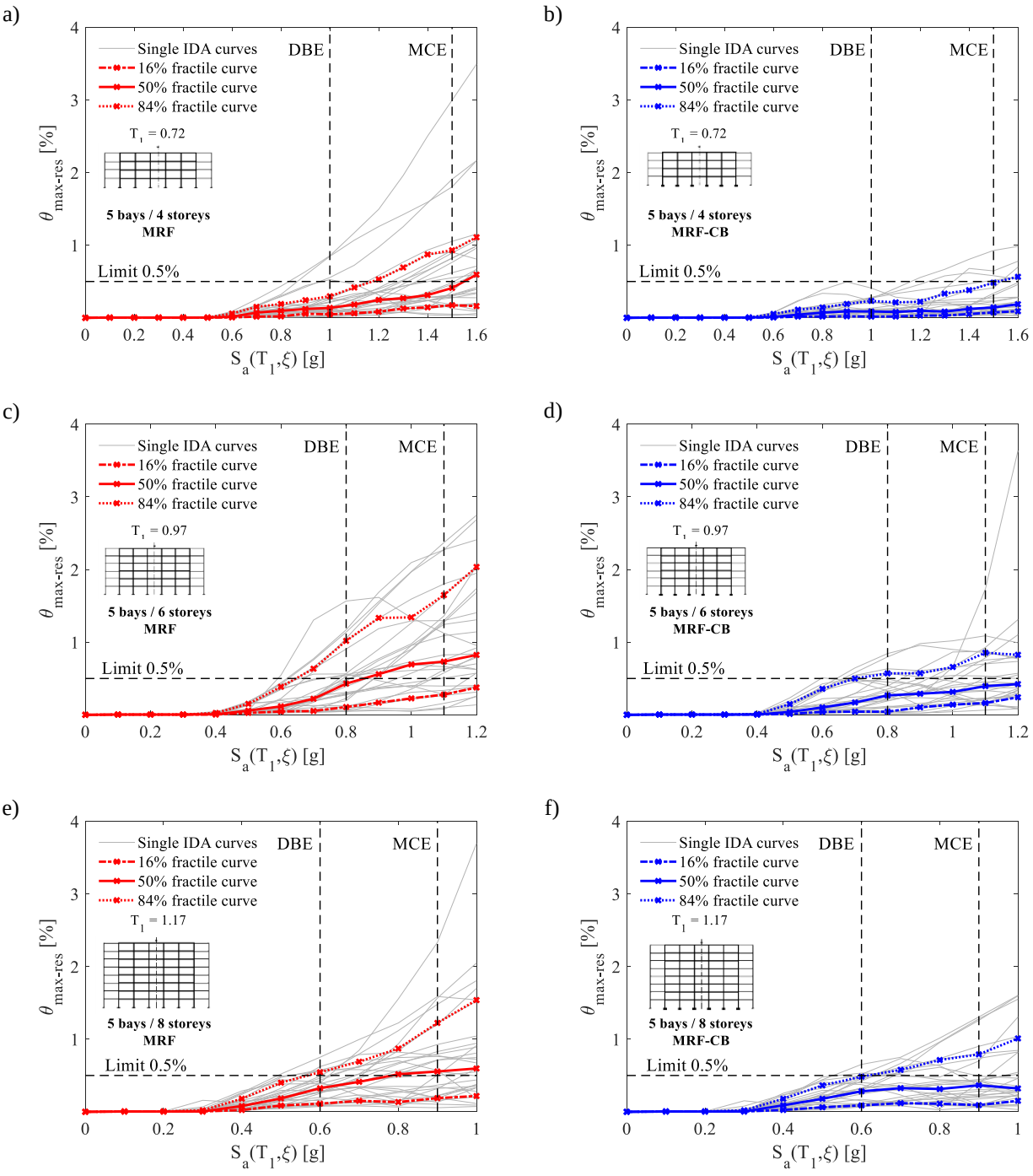

Figure A.2. IDA Results: Maximum residual interstorey drifts of the case-study frames: (a, b) 5-4; (c, d) 5-6; (e, f) 5-8.

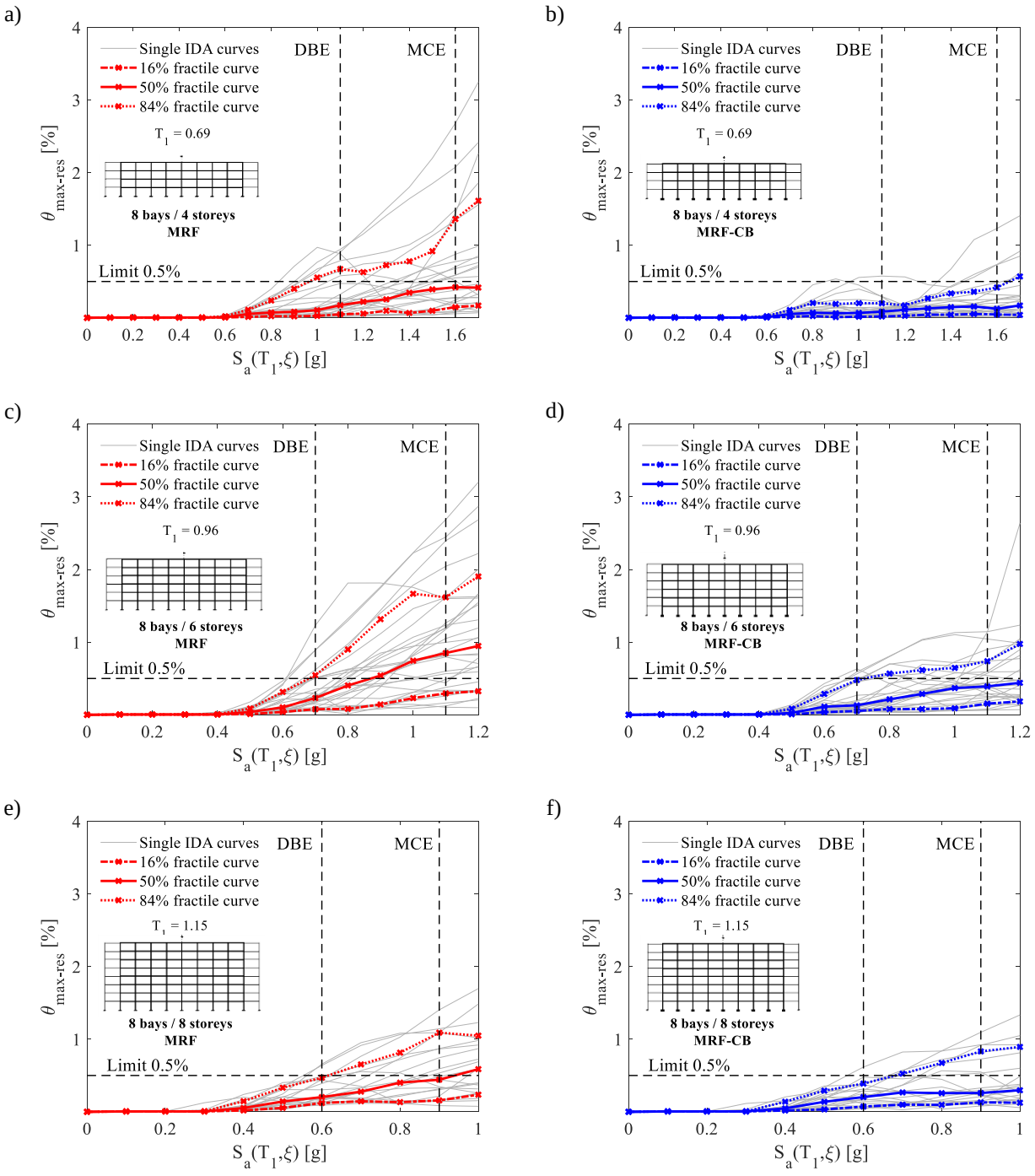

Figure A.3. IDA Results: Maximum residual interstorey drifts of the case-study frames: (a, b) 8-4; (c, d) 8-6; (e, f) 8-8.

REFERENCES

1 EN 1998-1, Eurocode 8: Design of structures for earthquake resistance – Part 1: General rules, seismic actions and rules for buildings, 2004, European Committee for Standardization, Brussels.

2 ASCE/SEI 7-16. Minimum design loads and associated criteria for buildings and other structures, American Society of Civil Engineers, 2017, Reston, USA.

3 ANSI/AISC 341-16 Seismic provisions for structural steel buildings, American Institute of Steel Construction, 2016, Chicago, USA.

4 Freddi, F., Novelli, V., Gentile, R., Veliu, E., Andonov, A., Andreev, S., Greco, F., Zhuleku, E. (2021). Observations from the 26th November 2019 Albania Earthquake: the Earthquake Engineering Field Investigation Team (EEFIT)

mission. Bulletin of Earthquake Engineering. https://doi.org/10.1007/s10518-021-01062-8.
5 Soong TT, Spencer Jr BF. Supplemental energy dissipation: state-of-the-art and state-of-the practise. Eng Struct 2002; **24**(3): 243–259.
6 Symans S, Charney FA, Whittaker AS, Constantinou MC, Kircher CA, Johnson MW, McNamara RJ. Energy Dissipation Systems for Seismic Applications: Current Practice and Recent Developments. J Struct Eng 2008; **134**(1): 3–21.
7 Freddi F, Tubaldi E, Ragni L, Dall'Asta A. Probabilistic performance assessment of low-ductility RC frames retrofitted with dissipative braces. Earthq Eng Struct D 2013; **42**(7): 993–1011.
8 Latour M, Piluso V, Rizzano G. Experimental analysis on friction materials for supplemental damping devices, Constr Build Mater 2014; **65**: 159–176.
9 Dall'Asta A, Tubaldi E, Ragni L. Influence of the non-linear behavior of viscous dampers on the seismic demand hazard of building frames. Earthq Eng Struct D 2016; **45**(1): 149–169.
10 Latour M, D'Aniello M, Zimbru M, Rizzano G, Piluso V, Landolfo R. Removable friction dampers for low-damage steel beam-to-column joints. Soil Dyn Earthq Eng 2018; **115**: 66–81.
11 Freddi F, Tubaldi E, Zona A, Dall'Asta A. Seismic performance of dual systems coupling moment-resisting and buckling-restrained braced frames. Earthq Eng Struct D 2020. DOI: 10.1002/eqe.3332.
12 Colajanni P, La Mendola L, Monaco A, Pagnotta S. Design of RC joints equipped with hybrid trussed beams and friction dampers. Eng Struct 2021; **227**, https://doi.org/10.1016/j.engstruct.2020.111442
13 Dall'Asta A, Leoni G., Micozzi F., Gioiella L., Ragni L. A resilience and robustness-oriented design of base-isolated structures: the new Camerino University Research Center. Frontiers in Built Environment 2020; **6** 50. https://doi.org/10.3389/fbuil.2020.00050.
14 Mokhtari M, Naderpour H. Seismic resilience evaluation of base-isolated RC buildings using a loss-recovery approach. B Earthq Eng 2020; **18**(10): 5031–5061.
15 De Domenico D, Tubaldi E, Takewaki I, Karavasilis T, Dall'Asta A, Lavan O. Editorial: Recent Advances and Applications of Seismic Isolation and Energy Dissipation Devices. Frontiers in Built Environment 2020; **6**: 126.
16 D'Aniello M, Tartaglia R, Costanzo S, Landolfo R. Seismic design of extended stiffened end-plate joints in the framework of Eurocodes, J Constr Steel Res 2017; **128**: 512–27.
17 Francavilla AB, Latour M, Piluso V, Rizzano G. Design of full-strength full-ductility extended end-plate beam-to-column joints. J Constr Steel Res 2018; **148**: 77–96.
18 Tartaglia R, D'Aniello M, Landolfo R. The influence of rib stiffeners on the response of extended end-plate joints. J Constr Steel Res 2018; **148**: 669–690.
19 Tartaglia R, D'Aniello M, Rassati GA, Swanson JA, Landolfo R. Full strength extended stiffened end-plate joints: AISC vs recent European design criteria. Eng Struct 2018; **159**: 155–71.
20 Tartaglia R, D'Aniello M, Zimbru M, Landolfo R. Finite element simulations on the ultimate response of extended stiffened end-plate joints. Steel Compos Struct 2018; **27**: 727-745.
21 Tartaglia R, D'Aniello M, Rassati GA. Proposal of AISC-compliant seismic design criteria for ductile partially-restrained end-plate bolted joints. J Constr Steel Res 2019; **158**: 364–383.
22 Tartaglia R, D'Aniello M, Zimbru. Experimental and numerical study on the T-Stub behaviour with preloaded bolts under large deformations. Struct 2020; **27**:2137-2155.
23 Latour M, Rizzano G. Full strength design of column base connections accounting for random material variability. Eng Struct 2013; **48**: 458–71.
24 Latour M, Rizzano G. A theoretical model for predicting the rotational capacity of steel base joints. Eng Struct 2013; **91**: 89–99.
25 Rodas PT, Zareian F, Kanvinde A. Hysteretic model for exposed column-base connections. J Struct Eng 2016; **142**(12): 1–14.
26 MacRae GA, Urmson CR, Walpole WR, Moss P, Hyde K, Clifton GC. Axial Shortening of Steel Columns in Buildings Subjected to Earthquakes. Bulletin of The New Zealand Society for Earthq Eng 2009; **42**(4): 275–287.
27 Elkady A, Guell G, Lignos DG. Proposed methodology for building-specific earthquake loss assessment including column residual axial shortening. Earthq Eng Struc Dyn 2020; **49**: 339–355.
28 Grigorian CE, Yang TS, Popov EP. Slotted bolted connection energy dissipators. Earthq Spectra 1993; **9**(3): 491–504.
29 MacRae GA, Clifton GC, Mackinven H, Mago N, Butterworth JW, Pampanin S. The Sliding Hinge Joint Moment connection, Bulletin of The New Zealand Society for Earthq Eng 2010; **43**(3): 202–212.
30 Latour M, Piluso V, Rizzano G. Experimental analysis of beam-to-column joints equipped with sprayed aluminium friction dampers. J Constr Steel Res 2018; **146**: 33–48.
31 Ramhormozian S, Clifton GC, Latour M, MacRae GA. Proposed simplified approach for the seismic analysis of multi-storey moment resisting framed buildings incorporating friction sliders. Buildings 2019; **9**(5): 130.
32 Borzouie J, MacRae GA, Chase JG, Rodgers GW, Clifton GC. Experimental studies on cyclic performance of CB strong axis – aligned asymmetric friction connections. J Struct Eng (ASCE) 2016; **142**(1): 1–10.
33 McCormick J, Aburano H, Nakashima M. Permissible residual deformation levels for building structures considering both safety and human elements. 14th World Conf Earthq Eng 2008, Beijing, China.

34 MacRae GA, Clifton GC. Low Damage Design of Steel Structures, Steel Innovations 2013 Workshop, Christchurch, New Zealand.
35 Chancellor NB, Eatherton MR, Roke DA, Akbas T. Self-Centering Seismic Lateral Force Resisting Systems: High Performance Structures for the City of Tomorrow. Buildings 2014; **4**: 520–548.
36 Ricles J, Sause R, Garlock M, Zhao C. Posttensioned Seismic-Resistant Connections for Steel Frames. J Struct Eng 2001; **127**(2): 113–121.
37 Christopoulos C, Filiatrault A, Uang C-M, Folz B. Posttensioned energy dissipating connections for moment-resisting steel frames. J Struct Eng 2002; **128**(9): 1111–20.
38 Kim HJ, Christopoulos C. Friction damped posttensioned self-centering steel moment-resisting frames. J Struct Eng 2008; **134**(11): 1768–79.
39 Vasdravellis G, Karavasilis TL, Uy B. Large-scale experimental validation of steel posttensioned connections with web hourglass pins. J Struct Eng 2012; **139**: 1033–1042.
40 Takamatsu T, Tamai H. Non-slip-type restoring force characteristics of an exposed-type CB. J Constr Steel Res 2005; **61**(7): 942–961.
41 Ikenaga M, Nagae T, Nakashima M, Suita K. Development of CBs having self-centering and damping capability. 5th Int. Conf. on Behaviour of Steel Struct. in Seismic Areas 2006, Yokohama, Japan.
42 Mackinven H, MacRae GA, Pampanin S, Clifton GC, Butterworth J. Generation four steel moment frame joints. 8th Pacific Conf on Earthq Eng 2007, Singapore.
43 Chou CC, Chen JH. Analytical model validation and influence of CBs for seismic responses of steel post-tensioned self-centering MRF systems. Eng Struct 2011; **33**(9): 2628–2643.
44 Chi H, Liu J. Seismic behaviour of post-tensioned CB for steel self-centering moment resisting frame. J Constr Steel Res 2012; **78**: 117–130.
45 Yamanishi T, Kasai K, Takamatsu T, Tamai H. Innovative column-base details capable of tuning rigidity and strength for low to medium-rise steel structures. 15th World Conf. on Earthq. Eng. 2012, Lisbon, Portugal.
46 Freddi F, Dimopoulos CA, Karavasilis TL. Rocking damage-free steel CB with Friction Devices: design procedure and numerical evaluation. Earthq Eng Struct Dyn 2017; **46**: 2281–2300.
47 Freddi F, Dimopoulos CA, Karavasilis TL. Experimental evaluation of a rocking damage-free steel CB with friction devices. J Struct Eng (ASCE) 2020; **146**(10): 04020217. DOI: 10.1061/(ASCE)ST.1943-541X.0002779.
48 Kamperidis V, Karavasilis TL, Vasdravellis G. Self-centering steel CB with metallic energy dissipation devices. J Constr Steel Res 2018; **149**: 14–30.
49 Wang XT, Xie CD, Lin LH, Li J. Seismic behaviour of self-centering concrete-filled square steel tubular (CFST) CB. J Constr Steel Res 2019; **156**: 75–85.
50 Latour M, Rizzano G, Santiago A, Da Silva L. Experimental response of a low-yielding, self-centering, rocking CB joint with friction dampers. Soil Dyn Earthq Eng 2019; **116**: 580–592.
51 Elettore E, Freddi F, Latour M, Rizzano G. Design and analysis of a seismic resilient steel moment resisting frame equipped with damage free self-centring column bases. J Constr Steel Res 2021; **179**: 106543
52 Moradi S, Alam MS. Lateral Load–Drift Response and Limit States of Posttensioned Steel Beam-Column Connections: Parametric Study. J Struct Eng 2017, **143**(7): 04017044.
53 Kamperidis VC, Papavasileiou GS, Kamaris GS, Vasdravellis G. Seismic collapse of self-centering steel MRFs with different column base structural properties. J Constr Steel Res 2020; **175**: 106364.
54 Herning G, Garlock MEM, Vanmarcke E. Reliability-based evaluation of design and performance of steel self-centring moment frames. J Constr Steel Res 2011; **67**: 1495–1505.
55 Mazzoni S. McKenna F. Scott MH, Fenves GL. OpenSEES: Open System for earthquake engineering simulation, Pacific Earthquake Engineering Research Centre (PEER) 2009, Univ. of California, Berkley, CA, Available at: http://opensees.berkeley.edu.
56 Vamvatsikos D, Cornell CA. Incremental Dynamic Analysis. Earthq Eng Struct Dyn 2002; **31**(3): 491–514.
57 Shinozuka M, Feng MQ, Kim H-K, Kim S-H. Non-linear static procedure for fragility curve development. J Eng Mech 2000; **126**(12): 1287–95.
58 EN 1993-1-8, Eurocode 3: Design of steel structures, Part 1-8: Design of steel structure: General rules and rules for buildings, 2005, European Committee for Standardization, Brussels.
59 Cavallaro GF, Francavilla AB, Latour M, Piluso V, Rizzano G. Cyclic behaviour of friction materials for low yielding connections. Soil Dyn Earthq Eng 2018; **114**: 404–423.
60 Cavallaro GF, Latour M, Francavilla AB, Piluso V, Rizzano G. Standardised friction damper bolt assemblies time-related relaxation and installed tension variability. J Constr Steel Res 2018; **141**: 145–155.
61 D'Aniello M, Cassiano D, Landolfo R. Monotonic and cyclic inelastic tensile response of European preloadable gr10.9 bolt assemblies. J Constr Steel Res 2016; **124**: 77-90.
62 D'Aniello M, Tartaglia R, Cassiano D. Experimental investigation of the inelastic tensile behaviour of non-preloadable grade 8.8 bolts. Ingegneria Sismica 2020 XXXVII(2):92-110
63 EN 1993-1-1, Eurocode 3: Design of steel structures, Part 1-1: Design of steel structures: Design of joints, 2005, European Committee for Standardization, Brussels.
64 Lignos D, Krawinkler H. Deterioration Modelling of Steel Components in Support of Collapse Prediction of Steel

Moment Frames under Earthquake loading. J Struct Eng 2011; **137**: 1291–1302.
65 Charney F, Downs W. Modelling procedures for panel zone deformations in moment resisting frames. Connections in Steel Struct. V 2004. ESSC/AISC Workshop, Amsterdam.
66 Foutch DA, Yun S-Y. Modeling of steel moment frames for seismic loads. J Constr Steel Res 2002; **58**: 529–564.
67 Iervolino I, Galasso C, Cosenza E. REXEL: Computer aided record selection for code-based seismic structural analysis. B Earthq Eng 2010; **8**: 339–362.
68 Cornell, CA, Jalayer F, Hamburger RO, Foutch DA. Probabilistic Basis for 2000 SAC Federal Emergency Management Agency Steel Moment Frame Guidelines. J Struct Eng 2002; **128**:526-533.